Title

Predictive simulation of non-steady-state transport of gases through rubbery polymer membranes

Authors

Soniat, Marielle
Tesfaye, Meron
Brooks, Daniel
et al.

Publication Date

2018

DOI

10.1016/j.polymer.2017.11.055

Peer reviewed

Predictive simulation of non-steady-state transport of gases through rubbery polymer membranes

Marielle Soniat,[a,b] Meron Tesfaye[c,d], Daniel Brooks,[e] Boris Merinov,[e] William A. Goddard, III,[e] Adam Z. Weber [a,c] and Frances A. Houle*[a,b]

[a] Joint Center for Artificial Photosynthesis, Lawrence Berkeley National Laboratory, Berkeley, CA 94720

[b] Chemical Sciences Division, Lawrence Berkeley National Laboratory, Berkeley, CA 94720

[c] Energy Storage and Distributed Resources Division, Lawrence Berkeley National Laboratory, Berkeley, CA 94720

[d] Department of Chemical and Biomolecular Engineering, University of California, Berkeley, CA 94720

[e] Materials and Process Simulation Center (MSC), Beckman Institute, California Institute of Technology, Pasadena, CA, 91125

* Author to whom correspondence should be addressed. fahoule@lbl.gov, (510) 495-8135.

Abstract

A multiscale, physically-based, reaction-diffusion kinetics model is developed for non-steady-state transport of simple gases through a rubbery polymer. Experimental data from the literature, new measurements of non-steady-state permeation and a molecular dynamics simulation of a gas-polymer sticking probability for a typical system are used to construct and validate the model framework. Using no adjustable parameters, the model successfully reproduces time-dependent experimental data for two distinct systems: (1) O_2 quenching of a phosphorescent dye embedded in poly(n-butyl(amino) thionylphosphazene), and (2) O_2, N_2, CH_4 and CO_2 transport through poly(dimethyl siloxane). The calculations show that in the pre-steady-state regime, permeation is only correctly described if the sorbed gas concentration in the polymer is dynamically determined by the rise in pressure. The framework is used to predict selectivity targets for two applications involving rubbery membranes: CO_2 capture from air and blocking of methane cross-over in an aged solar fuels device.

Keywords: rubbery polymers; reaction-diffusion modeling; gas transport

Nomenclature: List of symbols

Symbol	Meaning	Units
A	area	m^2
$B + 1$	ratio of intensities	--
dx	distance in x	m
D	diffusivity	m^2/s
h	Planck constant	J s
I_0	intensity of light emission in absence of O_2	-- *
I_{eq}	intensity of light emission at a constant $[O_2]$	-- *
$I(t)$	time-dependent light intensity	-- *
J	flux through membrane	$mol/(m^2\ s)$
k_B	Boltzmann constant	J/K
k_{ads}	pseudo-first order rate constant for adsorption	s^{-1}
k_{bub}	zeroth order rate constant for CH_4 to enter gas phase	mol/(L s)
k_{coll}	rate constant for collision of gases with the surface	s^{-1}
k_{des}	rate constant for desorption from a surface	s^{-1}
k_{ex}	pseudo-first order rate constant for excitation of PtOEP	s^{-1}
k_{hyd}	zeroth order rate constant for CH_4 to enter gas phase	mol/(L s)
k_{nr}	rate constant for radiative decay of PtOEP	s^{-1}
k_{prod}	zeroth order rate constant for production of CH_4	mol/(L s)
k_q	rate constant for quenching of PtOEP by O_2	L/(mol s)
k_r	rate constant for emission of photons from PtOEP	s^{-1}
k_{TTA}	rate constant for TTA	L/(mol s)
l	thickness of the membrane	m
m_w	molecular mass	kg/mol
n	amount of gas	mol
n_{max}	maximum amount of gas	mol
N_{Av}	Avogadro's number	molecules/mol
P_m	permeability of the membrane	$(mol\ m)/(m^2\ s\ Pa)$ for gas phase
		m^2/s for liquid phase
p_{ds}	downstream pressure	Pa
p_{O2}	external partial pressure of O_2	Pa
p_{up}	upstream pressure	Pa
Δp	difference between upstream and downstream pressures	Pa
r_{sun}	ratio of current sunlight level to maximum sunlight level	---
R	universal gas constant	J/(mol K)
R_{AB}	encounter distance	m
S	solubility	mol/(L Pa) for gas phase
		(mol/L)/(mol/L) for liquid phase
t	time	s

T	temperature	K
V	volume	m^3
V_{ds}	downstream volume	m^3
x	position	m
Z	collision frequency	s^{-1}
μ	sticking probability	--
ν_L	frequency of exciting light	m
π	pi	--
ρ	mass density	kg/m^3
σ_a	absorption cross section	m^2
τ	lifetime of ^{3}PtOEP in the presence of a constant $[O_2]$	s
τ_0	lifetime of ^{3}PtOEP in the absence of O_2	s
ϕ_P	phosphorescence quantum yield	--
χ	rate	mol/(L s)
ω_L	energy density	J/m^2
$[gas_{(p)}]$	concentration of a gas within the polymer	mol/L
$[O_{2(p)}]_{eq}$	concentration of O_2 within the polymer at equilibrium	mol/L
$[O_{2(p)}](x,t)$	concentration of O_2 within the polymer as a function of position and time	mol/L
[PtOEP]	total concentration of PtOEP	mol/L
$[^3PtOEP]_{init}$	initial concentration of excited-state PtOEP	mol/L

* All reported intensities are normalized and so unitless.

I. Introduction

Permeant transport through a polymer membrane is driven by differences in pressure, concentration, temperature, and, if it is a polyelectrolyte, the electrical potential across it.[1] The most common model is the solution-diffusion model for steady-state, which is defined in terms of the permeability, P_m. The permeability is the product of the Henry's Law solubility, S, and diffusivity, D, i.e. $P_m = S \times D$.[2] Models with a high level of detail concerning the physical nature of uptake and permeation are not generally available. Such models are valuable for their predictive character and their ability to provide scientific insight. This work builds a foundation for the development and use of these more detailed models in the study of transport through polymers.

Polymeric membrane materials fall into two basic classes, highly permeable rubbers with low glass transition temperatures (Tg) and weakly permeable glasses with high Tg. The solution-diffusion model applies to both. The physical processes that take place in the polymer bulk do not depend on whether the permeant was initially present as a component of a liquid or in the gas phase. The details of the process of uptake into the membrane, on the other hand, are likely to depend on permeant phase. The solution-diffusion model assumes that no matter what the source of the permeant, its rate of uptake at the polymer interface is much faster than diffusion through the polymer bulk,[3] and therefore is not rate limiting. Molecular dynamics simulations and kinetics models using parameterized schemes have provided important insights to the detailed nature of uptake and permeation for ion-conducting, phase-separated perfluorosulfonic-acid polymers.[4-5] This level of physical detail, however, is not available for most membrane systems.

Steady-state permeation as described by the solution-diffusion model is relevant to many applications using polymeric membranes such as purification and electrolyzer systems, but not to those in which permeant concentrations and other operating conditions such as temperature vary significantly with time. Examples are gas sensor and intermittent gas separations systems, electrolyzers using electricity from renewable sources, or photoelectrochemical systems that use sunlight to convert components of air and water into fuels. The membrane composition and structure required for each of these applications varies, and at our current level of understanding the physical details governing time-dependent membrane performance cannot be assumed to be as simple to capture as they are by the solution-diffusion model. To begin to develop a

description of membrane behaviors far from steady state, we focus in this study on one extreme – inert gases permeating a rubbery polymer. Our basic model is constructed in a manner that enables it to be extended to more complex situations such as mixed-matrix membranes, metal foam separators, permeant-induced ageing, permeation of mixtures whose transport properties through the membrane are not independent of each other, and permeation under variable temperature conditions. The ability to model such situations predictively allows membrane architectures well-suited for time-varying applications to be developed.

The rubbery, non-interacting regime applies to membranes for gas sensors and certain gas separators. We consider time-dependent permeation in two configurations: (1) reversible permeation of gases into a gas-sensor system, and (2) pre-steady-state transport through a gas separator. Time-dependent data for a sensor system have been reported in the literature.[6-8] For the present work, we examine a comprehensive data set describing quenching of phosphorescence of a dye in a series of rubbery polymers by O_2 and have used them to develop and validate a basic model framework. Time-dependent gas-separator data obtained under well-controlled conditions are scarce, so we have measured non-steady-state permeation of gases over a range of pressures through a rubbery polymer, polydimethylsiloxane (PDMS) for this work. The gases - O_2, N_2, CO_2, and CH_4 - are selected to span a range of gas solubilities and nature of interaction with the polymer chains. We have examined aspects of uptake by using molecular dynamics simulations to estimate the fraction of CO_2-PDMS collisions that result in adsorption or absorption. Using these data, a multiscale, reaction-diffusion model framework has been constructed that successfully reproduces both sensor and separator data with no adjustable parameters, and reveals several aspects of the permeation process that are kinetically significant. Because it is predictive, the model is useful to examine functional systems. As an example, we describe simulation results for use of rubbery membranes to separate gas mixtures, and product crossover between cathode and anode chambers during a diurnal cycle of a solar-driven photoelectrochemical CO_2 reduction system. The latter case is applicable to a system in which the membrane has become rubbery due to prolonged exposure to CO_2.

II. Methods and Materials

Three separate methodologies have been combined in the present study: stochastic reaction-diffusion simulations, molecular-dynamics simulations, and gas-permeation measurements. The materials set considered in this work is shown in Figure 1.

A. Reaction-diffusion simulations

The goal of this work is to develop a predictive model whose simulation outputs can be compared directly to experimental data. This requires that all simulation inputs (system geometry, rate constants and concentrations of all reactants and products) be measured

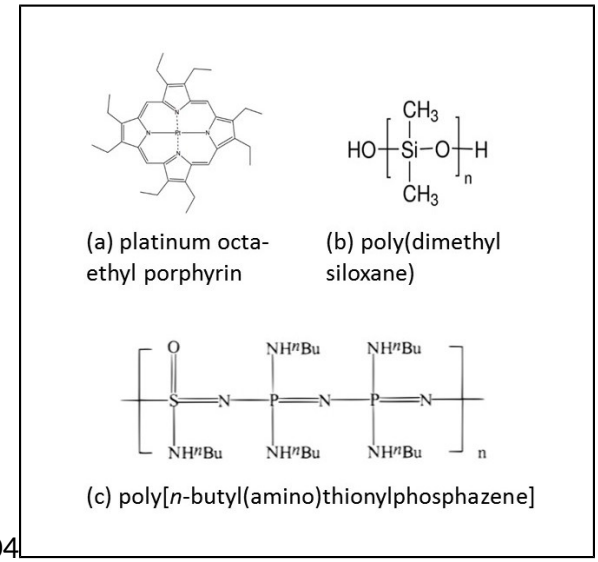

Figure 1. Chemical structures of the phosphorescent dye (a) platinum octa-ethyl porphyrin (PtOEP), and the polymers (b) poly(dimethyl siloxane) (PDMS) and (c) poly[n-butyl(amino)thionylphosphazene] (C4PTP) investigated in this work.

experimentally, calculated by molecular dynamics simulations, or derived from established theory. The simulation reaction-diffusion code used in this study incorporates stochastic methods, a type of kinetic Monte Carlo that produces an accurate timebase.[9-10] It provides a rigorously accurate solution to the master equation for Markov systems, and is a useful alternative to coupled differential equation integrators for complex materials systems. It is particularly well-suited for systems that require detail at both nanoscale and macroscale dimensions, and involve large dynamic ranges in rates. The open access code package is

Kinetiscope.[11] Details on its computational methodology and applications to various types of condensed organic phase reaction-diffusion systems are described in previous publications.[12-17] The basic framework used in this work is a 1-dimensional reaction-diffusion system comprising a stack of micro-scale compartments to represent the polymer bulk, and source and receiver compartments separated by 1-nm-thick interfacial regions from the membrane. The construction of the reaction-diffusion model is described in Section III.

B. Molecular Dynamics Simulations

In most continuum models, gas uptake and desorption at the surface of a polymer membrane are considered to be instantaneous, with bulk transport being the controlling factor in permeation rate. However, to build a predictive model, it is necessary to use physically-derived rate constants for all processes. The dynamics of gas-rubbery polymer collisions are not well studied, so we have selected CO_2 among the gases used in this work, N_2, O_2, CH_4, and CO_2, for a thorough investigation of the uptake process using molecular dynamics (MD) simulations. All of the gases are weakly interacting with the polymers they permeate, so we assume that the sticking coefficient obtained from the study of CO_2 can be applied to all the gases studied in this work.

Simulations are performed using the Desmond MD simulation package[18-20] and the OPLS-2005 force field.[21] A time-step of 1 fs is used for short-range interactions and a 3 fs time-step is used for long-ranged interactions. Long-ranged electrostatics are computed using the Ewald summation. A short-ranged Coulomb cutoff of 9 Å is used. Center of mass motion is removed at each time step in the adsorption simulations.

The initial PDMS structure is generated using standard protocols in polymer construction. The initial low-density (ρ = 0.0245 kg/m^3) structure is created using an amorphous builder. This polymer structure has 25 chains of PDMS of 100-monomer length, for a total of 25,053 atoms. To ensure that there are no overlapping atoms in the structure, 100 steps of energy minimization and 10 ps of dynamics in the NVT ensemble[22] at 10 K are performed (using a time constant of 0.1 ps for the thermostat). The density of the structure is increased by running 500 ps of dynamics in the NPT ensemble using the algorithm of Martyna, Tobias, and Klein (MTK) with a 1 ps time constant for the barostat.[23] To ensure entanglement of the polymer chains, a Scaled Effective Solvent (SES)[24] equilibration step is performed in which long-ranged van der Waals and Coulomb interactions scaled to 20% of their original values, and dynamics are run for 2000

ps in the NVT ensemble with a Nosé-Hoover thermostat. Finally, with van der Waals and electrostatic interactions at their full strength, energy minimization is performed for 300 ps and the lattice parameters of the structure are again relaxed with 200 ps of NPT dynamics.

The above procedure results in a roughly 70-Å thick slab of PDMS created with dimensions of 6.79 × 6.79 × 6.79 nm^3. This procedure results in a bulk density of ≈0.985 kg/m^3, which is above the experimental reference value of 0.970 kg/m^3,[25] but below the experimental sample densities of 1.06 to 1.08 kg/m^3 obtained in this study (see Section II.C.). To create a PDMS surface, the length of the cell is increased by 200 Å in the x-direction to generate a region of empty space. All polymer chains are kept intact. The surface is then equilibrated for 3000 ps in the NVT ensemble using the Berendsen thermostat at 300 K. The density near the surface is reduced to ≈0.94 kg/m^3 due to surface roughness. The instantaneous surface is designated using the Gaussian smoothing method of Willard and Chandler,[26] which is described more fully in the SI Section 1. The final, equilibrated structure and its instantaneous surface are shown in Figure 2.

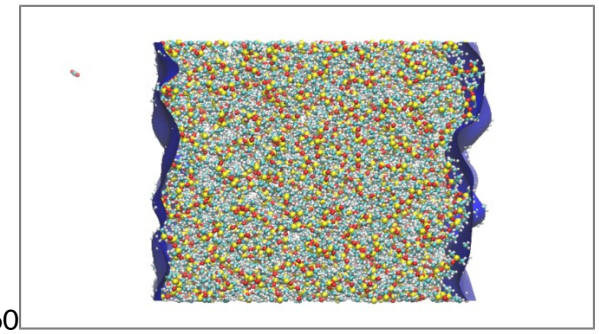

Figure 2. The structure of poly(dimethyl siloxane) (PDMS) in the molecular dynamics simulations. Hydrogen atoms are shown in white, carbon in light blue, oxygen in red and silicon in yellow. The instantaneous interface is shown in dark blue. The CO_2 molecule (upper left hand corner of the image) is sent towards the surface of the PDMS polymer structure for an adsorption simulation.

CO_2 absorption, adsorption, and desorption events are tracked using a procedure based on the molecular adsorption studies of Julin *et al.*[27-28] A CO_2 molecule is introduced at a distance of approximately 15 Å from the surface and is assigned a velocity from the Maxwell-Boltzmann distribution at 300 K, with the constraint that the x-component of the velocity vector lies within a 45-degree cone normal to the surface. After 100 ps of NVE simulation, the outcome (adsorption,

absorption, desorption) is recorded based on the position of the CO_2 molecule relative to the surface region, which is defined as points within 4 Å, *i.e.* twice the van der Waals radius, of the instantaneous surface. Justification of the 4-Å cutoff is given in the results section.

Experimental permeation measurements

Complete time-dependent permeation curves for several gases through PDMS were obtained in this work. To our knowledge such data have not been previously reported, and they are needed for accurate model construction and validation. Additional details are presented in the SI Sections 2 and 3.

Sample Preparation. PDMS samples are prepared using standard procedures. The PDMS base and a proprietary crosslinker (Sylgard 184, Dow Corning Corp., Auburn, MI) are mixed in a 10:1 ratio by weight. The PDMS solution is degassed to remove air bubbles and cast onto silicon wafers to the desired thickness *via* the spin-coating method. The polymer films are stored in deionized water until use. Prior to measurement, each sample is thoroughly dried and degassed. The thickness of the dry films is in the range of 163 to 165 μm, as measured by a micrometer (Mitutoyo, Aurora, IL). A helium gas displacement pycnometer (AccuPyc II 1340 from Micromeritics Instrument Corp., Norcross, GA) is used to measure the density, which ranges from 1.06 to 1.08 kg/m^3. The glass transition temperature is 149 ± 0.3 K, measured using differential scanning calorimetry (DSC800 Perkin Elmer, Waltham, MA).

Gas Permeation. A custom-built system is used for constant-volume gas-permeation experiments. A schematic is available in Reference [29]. Prior to the permeation experiment, gas is evacuated from the entire apparatus, a check for leaks is performed, and the measured permeabilities are corrected for any small pressure drifts. Upstream pressures of 119 to 835 kPa are tested. The upstream pressure is maintained at least two orders of magnitude greater than the downstream pressure during the measurements so that the pressure difference across membrane is effectively constant. The upstream pressure is monitored using a Honeywell STJE (Honeywell, Morris Plains, NJ) pressure transducer, which has a range of -2 to 7000 kPa and an accuracy of ±100 kPa.[30] The downstream pressure is monitored using a Baratron MKS (MKS Instruments, San Jose, CA) pressure transducer, which has a range of 0.1 to 1000 Pa and an accuracy of ±7 Pa.[31] The temperature of the system is maintained at 308 K in a water bath using an Alpha

immersion thermostat (Lauda, Delran, NJ). All gases, N_2, O_2, CH_4, and CO_2, (Praxair, Danbury, CT) are at least 99.9% pure and are used as received.

After the gas permeation process has reached steady state, the gas permeability of the membrane, P_m, is calculated from the gas flux, J, through membrane of thickness, l, due to a difference in partial pressure, Δp, across the membrane:

$$P_m = \frac{J\,l}{p_{up} - p_{ds}} = \frac{V_{ds}\,l}{\Delta p\,A\,RT}\left[\left(\frac{dp_{ds}}{dt}\right)_{SS} - \left(\frac{d\,p_{ds}}{dt}\right)_{leak}\right] \quad (1)$$

where V_{ds} is the downstream collection volume, A is the membrane area, R is the universal gas constant, T is the temperature, p_{ds} refers to the downstream pressure, p_{us} refers to the upstream pressure, and $(dp_{ds}/dt)_{SS}$ is the steady-state pressure rise, which is corrected for the leak rate $(dp_{ds}/dt)_{leak}$. At steady state, $P_m = D \times S$.

III. Development of a kinetic model for O_2 sorption and phosphorescent dye quenching in a sensor system

Detailed reaction-diffusion models for non-steady state transport in polymer membranes have not been reported previously, and development of a predictive description requires multiple independent types of time-dependent experimental measurements to validate it.[12, 14] There are few of these in the literature for any polymer type, however, a particularly useful set for rubbery polymers has been reported by Jayarajah and coworkers.[6-7] In this section, we describe how we developed the model for their measurements, quenching of a phosphorescent dye in a rubbery polymer by oxygen for a sensor application,[8] and compared predictions to experimental observations. The polymer used is poly(n-butyl (amino) thionyl phosphazene) (C4PTP). This polymer has a low Tg of 257 K and was studied at a thickness of 163 μm. The dye platinum octa-ethyl porphyrin (PtOEP) is dispersed in the polymer, and quenching of its laser-excited phosphorescence acts as an indicator of the internal concentration of O_2 gas. The structures of the C4PTP monomer and of PtOEP are shown in Figure 1 and the reaction mechanism and rate coefficients are summarized in Table 1.

	units	**PS**	Ref.	**C4PTP**	Ref.
$D(O_2)$	m^2/s	1×10^{-11}	[32] (a)	4.0×10^{-10}	[7]
$S(O_2)$	mol/(L Pa)	8.26×10^{-8}	[32] (a)	1.18×10^{-8}	[7]

$[O_{2(p)}]_{eq}$	mol/L	1.73×10^{-3}	this work	2.40×10^{-4}	this work
[PtOEP]	mol/L	0.0731	[33]	3.1×10^{-4}	[7]
$[^3PtOEP]_{init}$	mol/L	5.85×10^{-4}	this work	2.48×10^{-6}	this work
ϕ_P		0.54	[33]	0.54	this work
τ_0	μs	60	[33]	103	[7]
k_r	s^{-1}	8.33×10^3	[33]	3.9×10^3	this work
k_{nr}	s^{-1}	8.30×10^3	[33]	5.8×10^3	this work
k_{TTA}	$M^{-1}\ s^{-1}$	4×10^7	[33]	4×10^7	this work
k_q	$M^{-1}\ s^{-1}$	1.82×10^7	this work (b)	3×10^9	this work
k_{ex}	s^{-1}	-----		50	this work

(a) for amorphous, atactic polystyrene

(b) calculated from the reported pseudo-first order rate constant 3.20 x 10^4 s^{-1} reported in Ref. [33] and the expected concentration of O_2 in the polymer.

Table 1. Simulation inputs for phosphorescence quenching.

A. System Geometry

As shown in Figure 3, the membrane is represented as a set of 100 homogeneous compartments, each 1.63 μm thick, coupled by Fickian diffusion paths. An interfacial compartment of 1 nm thickness is provided at the gas-polymer interface to enable explicit description of adsorption, desorption and transfer of gases to and from the polymer bulk. The other side of the membrane is in contact with a glass substrate and so is not permeable. The area of the membrane is taken to be the footprint of the laser beam used for dye excitation, 2 mm by 1 mm.

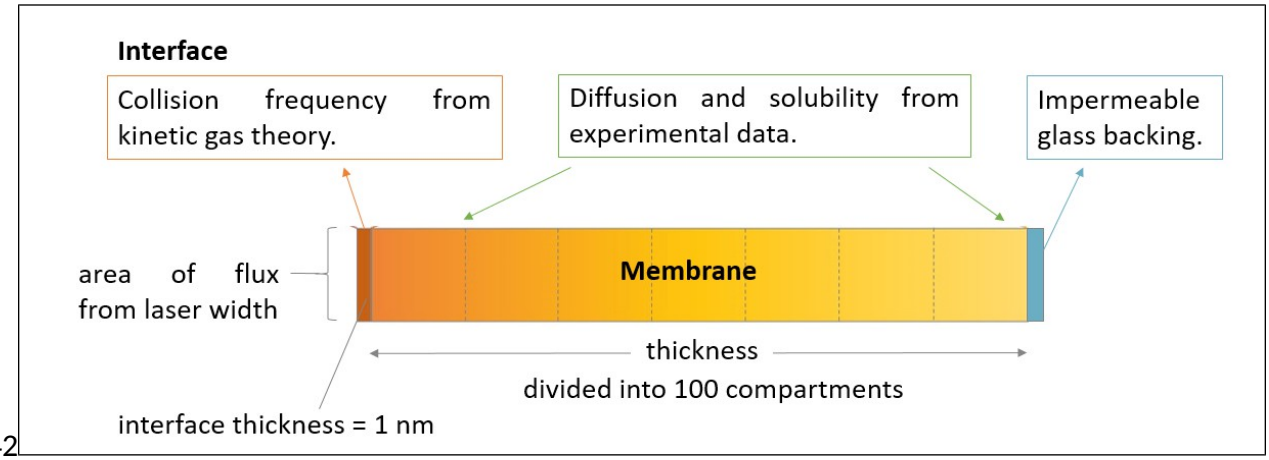

Figure 3. Overview of the multi-scale model for a sorption simulation. The membrane is divided into 100 compartments, plus one thin interfacial compartment. The area of flux is 2 mm by 1 mm, which is the area typical of a laser beam.

B. Gas-polymer interactions

The experimental diffusion coefficient is used for gas transport throughout the polymer, including the surface layers. The maximum concentration of a gas in the membrane is determined by its experimental Henry's Law solubility. Swelling was not reported for this system and is neglected in the simulations. When present, dynamic volume changes as the membrane swells must be included in the model. They will reduce solute concentrations and concentration gradients while increasing the diffusion coefficient, and their effect on permeation may vary with time.

Adsorption and desorption are represented as direct processes involving a gas molecule and a surface site, a description used in other studies.[15] Absorption is broken into two steps: sticking of the gas to the membrane surface and diffusion from the surface layer into the bulk. Sticking is represented as a reaction between a gas molecule and an empty surface site,

$$gas + site \xrightarrow{k_{ads}} gas - surface \qquad \text{(I)}$$

where the adsorption rate constant, k_{ads}, is the collision frequency of the gas with the surface, k_{coll}, times the sticking probability, μ,

$$k_{ads} = \mu k_{coll} = \mu(ZA) = \mu\left(\frac{p_{up}}{\sqrt{2\pi m_w k_B T}}\right)A \qquad (2)$$

and Z is the collision frequency per unit area, A is the experimental surface area, p is the upstream partial pressure of the gas, m_w is the molecular mass of the gas, k_B is Boltzmann's constant, and T is the temperature.[34] The sticking coefficient is initially assumed to be 0.1 (which is high but not unity since there is no information in the literature for this system); the sensitivity of the simulation to this value has been investigated and will be discussed in a later section. We use the generic term "site" because we assume that the gas molecules can physisorb to an atom type at the surface. The concentration of surface sites is assumed to be that of surface atoms in a liquid, 10^{14} atoms/cm^2.[35] Since the surface must be represented in a 3-dimensional compartment in Kinetiscope, the sites are distributed through a 1-nm thickness, giving a concentration of 1.66 mol/L. Once adsorbed, the gas molecule can diffuse from the interface layer to the adjacent bulk

polymer compartment. Desorption from the membrane is represented as detachment from a surface site, the reverse of Reaction I. Because the polymer and gas molecules are weakly interacting, we base the desorption rate constant on the breaking of a single van der Waals bond in the gas phase, such that k_{des} = 1.4 x 10^{11} s^{-1}.[36-37] The sensitivity of the simulation results to assumptions concerning the surface description is discussed below.

C. Kinetics of dye quenching

The dye is assumed to be uniformly distributed throughout the polymer bulk, and its excitation and deexcitation reactions are:

$$^3PtOEP \xrightarrow{k_{nr}} PtOEP \quad \text{(II)}$$

$$^3PtOEP \xrightarrow{k_r} PtOEP + photon \quad \text{(III)}$$

$$2\,^3PtOEP \xrightarrow{k_{TTA}} {}^3PtOEP + PtOEP \quad \text{(IV)}$$

$$^3PtOEP + O_{2(p)} \xrightarrow{k_q} PtOEP + O_{2(p)} \quad \text{(V)}$$

$$PtOEP \xrightarrow{k_{ex}} {}^3PtOEP \quad \text{(VI)}$$

where PtOEP is in the ground state, ^{3}PtOEP is in the first excited triplet state, and $O_{2(p)}$ is the oxygen gas within the polymer phase. These steps are the non-radiative decay, radiative decay, triplet-triplet annihilation (TTA), quenching, and excitation steps, respectively. In this section, we describe how the rate constants have been determined for these steps.

The photophysics have been determined from studies on PtOEP in polymer environments.[6-7, 33, 38] From the ground state, PtOEP absorbs at 380 nm and 547 nm to enter the first excited state;[38] greater than 99.9994% of PtOEP molecules excited to the first singlet state undergo intersystem crossing to the first excited triplet state ^{3}PtOEP.[33] Therefore, fluorescence from the singlet state is neglected. ^{3}PtOEP emits at 647 nm when well-dispersed in a clear polymer.[33, 38] For excited-state dye at high concentration or in solution with low viscosity, TTA may occur, in which one ^{3}PtOEP molecule quenches another and is itself excited back to the first excited singlet state. Because each excited singlet quickly relaxes to the first excited triplet we do not explicitly track the first excited singlet state in Reaction IV.[33]

Two types of experiments are examined to construct and validate a kinetic model for PtOEP photoprocesses. One determines the dye's phosphorescence lifetime using pulsed laser

excitation;[33, 38] the other determines the emission intensities of oxygen-free and oxygen-saturated polymer under continuous laser excitation.[7]

1. *Dye lifetime by pulsed laser excitation.*

Oxygen-free Environment. The phosphorescence lifetime, τ_0, phosphorescence quantum yield, ϕ_P, and TTA rate constant are determined experimentally for polystyrene (PS) in Reference [33] and are listed in Table 1. The rate constants for radiative decay, k_r, and non-radiative decay, k_{nr}, are calculated as

$$k_r = \frac{\phi_P}{\tau_0} \tag{3}$$

and

$$k_{nr} = \frac{1-\phi_P}{\tau_0} \tag{4}$$

Simulations of phosphorescence decay in PS using the reported rate constants were performed in order to establish the validity of the mechanism above (Rxn. II - IV). The intensity of emitted light, I, is calculated from the change in photon production over time. For these simulations, we can omit Reaction VI and start with a population of excited dye molecules. The intial excited-state dye population, $[^3\text{PtOEP}]_{init}$, can be calculated using

$$[^3PtOEP]_{init} = \frac{[PtOEP]\sigma_a\omega_L}{h\nu_L} \tag{5}$$

where [PtOEP] is the total concentration of dye molecules, σ_a is the absorption cross section of the dye at the exciting wavelength, ω_L is the energy density of the laser beam, h is Planck's constant, and ν_L is the exciting frequency. For the experiments of Bansal *et al*. (σ_a = 4.70 × 10^{-21} m^2; ω_L = 17.0 J/m^2; ν_L = 8.64 × 10^{14} s^{-1}; [PtOEP] = 0.0731 M), this calculation predicts that $[^3\text{PtOEP}]_{init}$ is 9.96 × 10^{-3} M. However, as shown in Figure 4, and explained in the SI, simulations using the reported rate constants are in good agreement with experiment only for $[^3\text{PtOEP}]_{init}$ equal to 5.85 × 10^{-4} M, which is 0.8% of the total dye concentration, [PtOEP] = 0.0731 M. The reason for this difference is not clear, but may reflect dye aggregation since clusters of PtOEP emit at 790 nm,[33, 38] which would not be detected in the experiments. Sensitivity studies for $[^3\text{PtOEP}]_{init}$ are described in the SI Section 4 and illustrated in Figure S1.

For C4PTP, only the lifetime and total dye concentration are reported. It is assumed that the unreported properties are the same as in PS, due to the dye being in a polymer environment in both cases. The rate constants for radiative and non-radiative decay are calculated from the assumed quantum yield and the experimentally measured phosphorescence lifetime. The initial excited-state dye population is assumed to be 0.8% of the total dye concentration, as it is in PS. All values related to the dye lifetime are listed in Table 1.

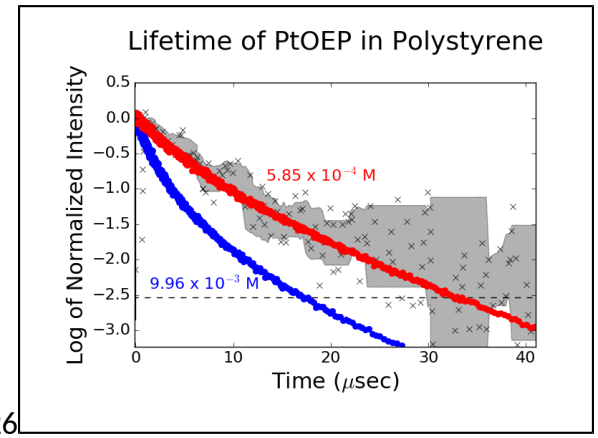

Figure 4. Simulated and experimental phosphorescence decay in air. The experimental data points from Ref. [33] are marked with black x's, and the gray region indicates the local standard deviation (over 11 data points). The dashed line indicates the lower detection limit of the instrument. The blue markers are for the simulation data using the reported value of $[^3\text{PtOEP}]_{init}$ = 9.96×10^{-3} M. The red markers are for a simulation using a reduced value of $[^3\text{PtOEP}]_{init}$ = 5.85×10^{-4} M.

Oxygen-containing Environment. Data for lifetimes in the presence of air are reported for PS and C4PTP. The introduction of oxygen in air opens a channel for quenching which competes with phosphorescence. The quenching rate constant, k_q, is calculated from the lifetime measured at a partial pressure of oxygen p_{O2} = 21 kPa, assuming that TTA is negligible. Then,

$$k_q = \frac{\frac{1}{\tau} - k_r - k_{nr}}{[O_{2(p)}]} \qquad (6)$$

where $[O_{2(p)}]$ is the concentration of oxygen gas within the polymer, and τ is the lifetime under ambient conditions. Simulations of PS using the reported quenching rate constant (see Table 1)

agree with experiment when $[^3\text{PtOEP}]_{init}$ = 0.8% of the total dye concentration. Sensitivity of the lifetime to k_q is discussed in SI Section 5 and illustrated in Figure S2.

2. Excitation rate constant from continuous excitation of the dye

The emission intensity is a result of the balance between excitation, radiative decay, and other forms of decay. Since the rate constants for all decay processes in the dye kinetics scheme are fixed, simulation of the emission intensity can be used to determine k_{ex}. However, the experimental data are reported as relative intensity values, rather than absolute intensities. The extrema in intensities are captured in the ratio $B = I_0/I_{eq} - 1$, where I_0 is the phosphorescence intensity in the absence of oxygen, and I_{eq} is the intensity for a constant concentration of O_2 consistent with p_{O2} = 21 kPa. The experimental value is $B = 74 \pm 6$. Simulations of the oxygen-free and oxygen-saturated steady-state scenarios are performed; then absolute and relative intensities are calculated. Values for the relative intensity B are plotted as a function of k_{ex} in Figure S3 in SI Section 6. The value of the ratio is quite insensitive to k_{ex} over a range of 1 to 100 s^{-1}, where B stays between 65 and 67. The median of k_{ex} = 50 s^{-1} is chosen, at which B = 66.

3. Time-dependent data.

The intensity over time, *I(t)*, was used by Jayarajah *et al*. to determine the solubility coefficient, *S*, and the diffusion coefficient, *D*, for O_2 in C4PTP using a two-parameter fit to the equation,

$$I(t) = \frac{I_0}{l}\int_0^l \frac{\left[O_{2(p)}\right]_{eq}}{1 + B\left[O_{2(p)}\right](x,t)}\,dx \qquad (7)$$

where

$$B = \frac{I_0}{I_{eq}} - 1 = 4\pi N_{Av}\tau_0 R_{AB} D S p_{O_2} \qquad (8)$$

where l is the membrane thickness, N_{Av} is Avogadro's number, τ_0 is the lifetime of PtOEP in the polymer environment in the absence of oxygen, $[O_{2(p)}](x,t)$ is the absolute concentration of O_2 within the membrane at position x at time t, and $[O_{2(p)}]_{eq}$ is the equilibrium concentration of O_2 within the membrane, which is equal to $S \times p_{O2}$.[6-7, 39] The equation above assumes that the dye is both distributed and excited homogeneously throughout the membrane (i.e. the sample is

optically thin). In the simulations, we also use a homogeneous dye distribution and assume homogeneous excitation.

The continuous excitation experiments were performed in two modes: (i) sudden replacement of N_2 with air, leading to sorption of O_2 and a decay in phosphorescence intensity, and (ii) sudden replacement of air by pure N_2, leading to desorption of O_2 and an increase in phosphorescence intensity. Because the pressure *vs* time data are not available to use as input to the simulations, the increase or decrease in oxygen partial pressure is assumed to be instantaneous in the simulation.

IV. Simulations of the O_2 sensor system

Simulations of emitted light intensity as O_2 sorbs into or desorbs from the polymer are used to calculate *I(t)* for comparison to experimental data. The absorption and desorption simulation results are compared with the experimental data in two ways: (i) dye kinetics are not simulated directly, but the total amount of O_2 predicted to be absorbed in the polymer in the simulation is used to calculate the expected *I(t)* using the reported intensity ratio of $B = 74$ and equations 7-8, and (ii) full simulation of the dye kinetics and the photons produced per unit time are directly compared to the experimental intensity over time. The use of two methods serves as a check on the internal consistency of the experimental data and on the validity of the reaction mechanism. The experimental value of B is chosen for comparison in method (i) because the estimation of k_{ex} introduces an additional discrepancy between simulation and experimental results.

The simulations predict the amount and distribution of oxygen gas within the membrane at all times. We compare the simulated O_2 amount to experiment, which does not measure O_2 in the film directly, by calculating n, the expected amount of O_2 in the membrane, from the experimental *I(t)* curve. We assume $dx = l$ in Equation 7, i.e. that the film is entirely uniform. The maximum amount of O_2 in the membrane, n_{max}, is found at equilibrium. $n_{max} = [O_{2(p)}]_{eq} \times V$, where $V = A \times l$. Then, rearranging Eq 7-8 gives

$$n = n_{max}\frac{1}{B}\left[\frac{B+1}{I(t)} - 1\right] \quad (9)$$

Simulation results for sorption and desorption are compared to experiment in Figure 5. The shape of the calculated curves is in good agreement with observations, but there are several quantitative differences. The initial rise in the simulated amount of O_2 in the polymer shown in Figure 5b is faster than that calculated from the experimentally measured *I(t)* using Equation 9. In the simulation, the amount of O_2 in the membrane compartments near the gas-polymer interface increases rapidly, and they become saturated with O_2. The rate of O_2 absorption then slows, limited by O_2 diffusion to the other side of the membrane. The reason for the difference between simulated and experimental amount of O_2 is unclear. One possibility is that the assumption of $dx = l$ in the calculation of the amount of O_2 from *I(t)* (either experimental or simulated) is not valid, which is supported by the fact that simulated and measured *I(t)* curves are in much closer agreement (Figure 5a).

(a)

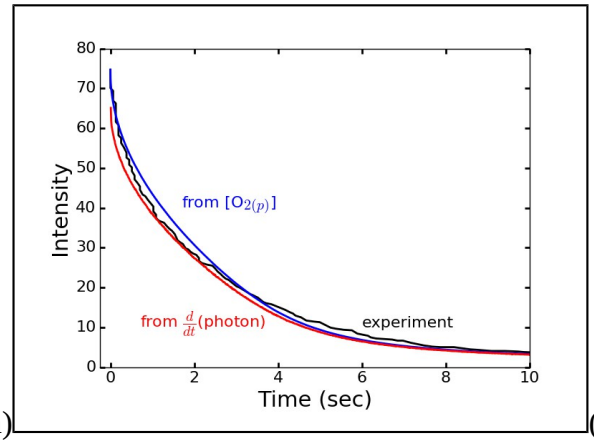

(b)

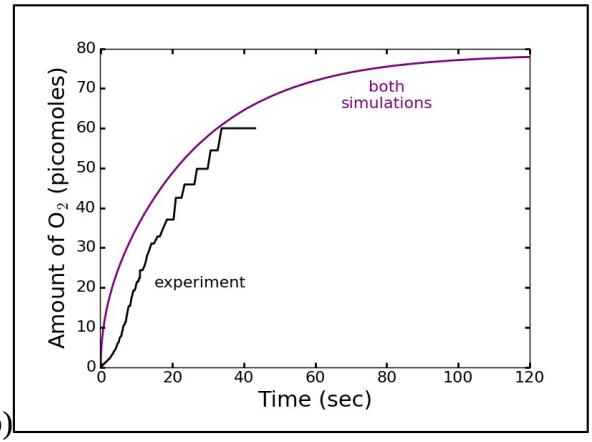

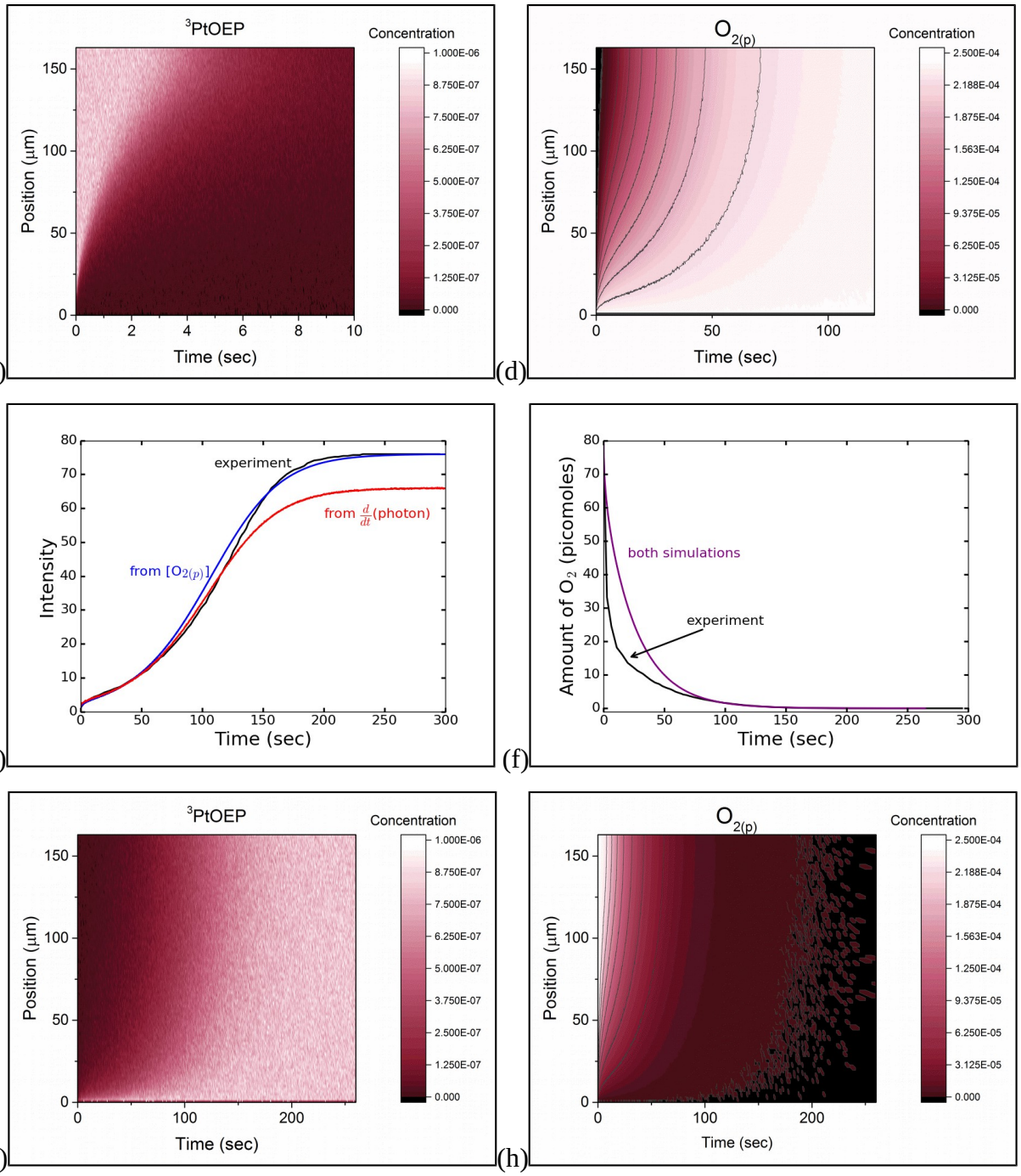

Figure 5. Results of simulation of laser-excited PtOEP and O_2 kinetics in C4PTP. In all the contour plots, darker colors represent lower concentration, and lighter colors represent higher concentration. Position is defined as 0 at the gas interface of the polymer. (a) *I(t)* when O_2 sorbs into the polymer, calculated from $O_{2(p)}$ with Eqn. 7 - 8 (blue) and from direct simulation of the dye photophysics (red); (b) The amount of $O_{2(p)}$ in the polymer as a function of time, comparing that calculated from the experimental data and both simulation types; (c) Contour plot of the concentration of ^{3}PtOEP through the polymer thickness during 10 s of sorption, showing complete quenching of phosphorescence; (d) Contour plot of the concentration of $O_{2(p)}$ through

the polymer thickness, reaching saturation after 120 s of sorption. (e) *I(t)* when O_2 desorbs from the polymer, calculated from $O_{2(p)}$ with Eqn. 7 - 8 (blue) and from direct simulation of the dye photophysics (red); (f) The amount of $O_{2(p)}$ in the polymer as a function of time, comparing that calculated from the experimental data and both simulation types; (g) The concentration of ^{3}PtOEP through the polymer thickness over time during desorption, with recovery of uniform phosphorescence by 200 s; (h) The concentration of $O_{2(p)}$ through the polymer thickness over time during desorption, uniformly reaching zero between 200 and 250 s.

Another possibility is the presence of inhomogeneities either in the polymer, dye distribution, or emission, that would lead to the same total phosphorescence intensity but no simple relationship between light emission and total O_2 in the film. This possibility was tested in two ways. First, a simulation in which dye is not present in the top quarter of the membrane gives a similar *I(t)* curve to experiment, showing that emission intensity is insensitive to spatial distribution of the dye and therefore to details of the O_2 kinetics. Second, altering the pressure profile of O_2 so that it does not instantaneously rise to p_{O2} = 21 kPa, but rather increases over several seconds, which is more similar to the experimental procedure, does not change the shape of the curve. Finally, the assumption that the sample is optically thin is tested via simulation in which only the dye in the top half of the membrane becomes excited; this situation results in an intensity profiles that dies off much more quickly than experiment. These considerations suggest that Equations 7-8 are qualitatively valid for estimating the full time dependence of O_2 absorption, but may not be quantitative in all cases.

Comparison of Figures 5a and c and Figures 5b and d also shows that while phosphorescence decays rapidly, the O_2 concentration in the membrane does not reach saturation until much later. In the sorption simulations, O_2 starts to reach the membrane compartments furthest from the interface after 2.0 sec. The concentration of ^{3}PtOEP is very small, and is fully quenched 8.1 sec after the introduction of O_2 to the polymer. However, the concentration of O_2 continues to rise for another 140 sec. Thus, there is not a one-to-one correspondence between the intensity and the O_2 concentration in the sensor film outside the range of 1 to 50 μmol/L of O_2., or an external partial pressure of 2 to 130 Pa, far below that used in this experiment.

The shape of the *I(t)* desorption curve for C4PTP is also captured well by the simulation (Figure 5e). There is an initial small but rapid increase in *I(t)* because the O_2 in the top membrane compartments desorbs in the first few seconds. From then until 50 s, there is slower rise in

intensity as O_2 diffuses from the lower compartments and desorbs, but the overall O_2 concentration within the membrane is still high enough to quench most of the dye. A more rapid increase in intensity ensues after 50 s, once the O_2 concentration is no longer in excess of that needed to quench ^{3}PtOEP. Finally, the maximum intensity is reached around 200 s, once all of the O_2 is removed from the polymer. The contour plots shown in Figures 5g and 5h, support this interpretation. The simulated O_2 content shown in Figure 5f is higher than that extracted from the *I(t)* measurements. This discrepancy may have the same origin as discussed above for the sorption case, Figure 5b.

Sensitivities of the simulation results to uncertainties have been thoroughly evaluated. Those for *D* and *S* are discussed in the SI Section 7 and shown in Figure S4. Those of the assumed properties of the gas-polymer interface are presented in Figures S5 and S6 and summarized here. Saturation of surface sites by O_2, assuming a sticking coefficient of 0.1, occurs within 10^{-21} seconds at 21 kPa. Reduction of the sticking coefficient to 10^{-17} has no effect on the O_2 profile, nor does increasing the sticking coefficient to 1. The concentration of adsorption or desorption sites can also be varied by 1 to 2 orders of magnitude with no effect. Alteration of the surface diffusion coefficient does not change the sorption results. Reduction, though not increase, of the interfacial diffusion coefficient does alter the desorption results, however. Finally, the desorption rate constant can also be reduced or increased by several orders of magnitude without altering the oxygen profiles. Because the simulation results are largely insensitive to surface kinetics at the rubbery polymer-inert gas interface, this type of simulation is not useful for exploring them, therefore we have used molecular dynamics simulations to gain more insight into the processes occurring at the surface.

V. Permeation of gases through a membrane separator: experiment and simulations

Having established a suitable reaction-diffusion framework as described in the preceding sections, we use it to examine the fully time-dependent permeation data obtained in this work, capturing not only steady-state permeation, but also the downstream pressure rise for steady-state and pre-steady-state regimes. In this section, we present the permeation measurements and simulations of them. In view of the insensitivity of sorption of gas by rubbery polymer sorption

to assumptions of gas sticking, we report molecular dynamics calculations to provide a description of this process for one system, thus avoiding an arbitrary guess in the model.

A. Measurements of time-dependent permeation through PDMS

In this study, the permeation of the gases N_2, O_2, CO_2, and CH_4 through PDMS is investigated at 308 K for various pressure gradients. The set of all experimental data is summarized in Table S1. The pressure *vs* time data are presented in the SI Section 8, and a selection of data is shown in Figure S7. The permeability is calculated from the rate of pressure increase downstream from the membrane when steady state is reached; differences due sample to sample variations are accounted for in the calculation of permeation via Equation 1. The permeability values as a function of pressure difference between source and receiver volumes are given in Figure 6. Each data point represents an average value of three or more different samples and measurements. The leak rate for each measurement is kept under 0.05% of the permeate flux. Propagated measurement error ranges from 1 to 4%. The error bars show the sample-to-sample variability, which is 10 to 20%. As can be seen in Figure 6, permeability shows no dependence on pressure gradient, indicating that the sorption isotherm is also linear. Permeation values for PDMS can vary with changes in base to cross-linker ratio, casting method, and annealing temperature. The measured values are consistent with previously measured values within experimental error and the sample-dependent variability of literature values.[40-42]{Merkel, 2000 #27} Higher pressure gradients (600 – 850 kPa) were also investigated, but with fewer experiments such that the variation between samples was not robustly characterized; so these data are omitted from Figure 6.

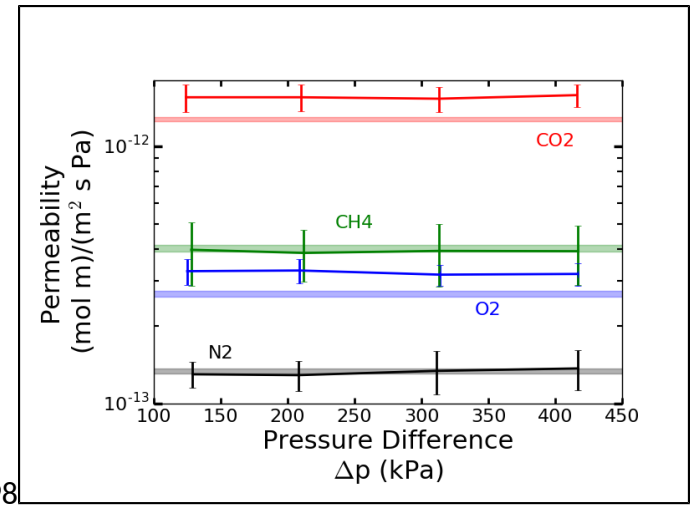

Figure 6. Comparison of experimental permeability to literature values. The literature values from Ref. [40] are shown with their standard deviation as the shaded regions.

B. Calculation of sticking probability of CO_2 on PDMS

Few data are available on sticking coefficients to of weakly interacting gases to PDMS or other rubbery polymers; therefore, we use molecular dynamics simulations to estimate reasonable values. We found that the sticking process is not kinetically limiting during construction of the permeation model for PDMS, similar to the finding for O_2 in C4PTP, so we have performed calculations for a single gas, CO_2, and assume that its sticking coefficient on PDMS is applicable to the other gases investigated. A series of 250 simulations of CO_2 impacts onto a PDMS surface was performed, and the results are shown in Figure 7 and summarized in Table 2. Some care must be taken in how the classification of type of event is interpreted: the distinction between an adsorbed and absorbed molecule is arbitrary, especially for atoms just below the interface, and the fate of molecules adsorbed on the surface is not clear from the finite simulation time. Thus, sticking in these simulations has a lower bound of 30%, equal to the fraction of absorbed molecules, and an upper bound of 50%, equal to the fraction of absorbed plus adsorbed molecules. The minimum sticking coefficient of 30% is used in the reaction-diffusion simulations for all gas molecules.

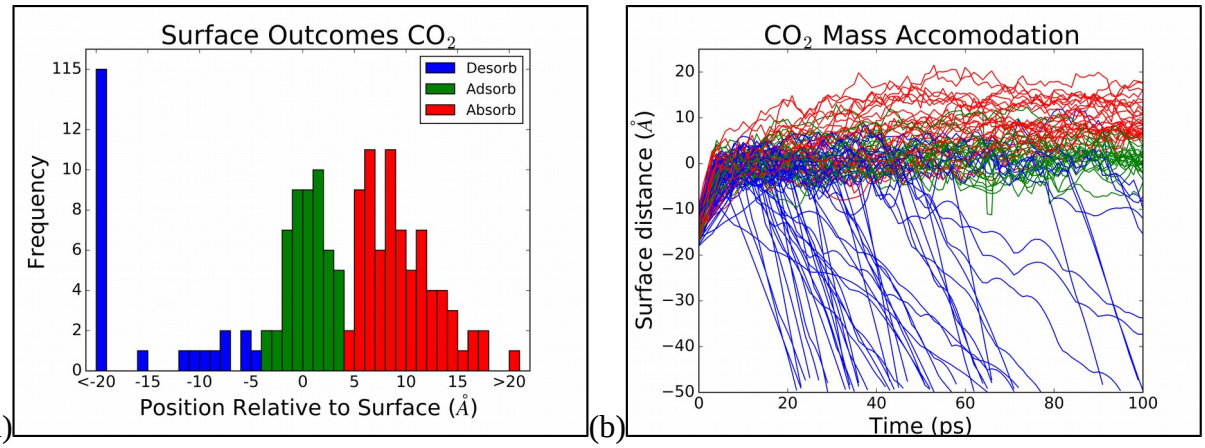

(a) (b)

Figure 7. Results of molecular dynamics simulations for CO_2 sticking to PDMS. The surface is defined as position 0 with positive position indicating the region occupied by polymer and negative position indicating the empty region. Absorbed molecules are plotted in red, adsorbed molecules in green, and scattered and desorbed molecules in blue. (a) Histogram showing the distribution of outcomes from all 250 simulations. Note that the far left blue bar represents desorption in 115 simulations. (b) Distance from the final Willard surface as a function of time for 100 randomly selected trajectories.

Events	**Absorb**	**Adsorb**	**Desorb**	**Total**
Number	75	50	125	250
Percent	30	20	50	100

Table 2. Results of Molecular Dynamics study of sticking of CO_2 to a PDMS surface.

The most similar system that has been studied experimentally is the scattering of the O_2 gas from the surface of the hydrocarbons squalane and dodecane.[43] At incident energies of 8 kJ/mol, twice the average kinetic energy for gas molecules in this study, the oxygen molecules fully transfer their excess energy to the hydrocarbon surface,[43] indicating a sticking probability near 100%. A MD study of carbon dioxide[44] colliding with hydrocarbon self-assembled monolayers (SAMs) also shows a large sticking probability of ≈70% when the SAMs are terminated with -CH_3 or -OH functional groups. The sticking probability falls to ≈40% for SAMs terminated with -CF_3. The reason for such a high sticking probability is explained in a MD study of argon colliding with hydrocarbon SAMs terminated with -CH_3 and -CF_3. The SAMs terminated with -CH_3 are able to redistribute the energy of the incoming molecule on the same timescale as the impact of the atom with the surface by recruiting a large number of low-frequency (inter-chain) vibrational modes; the SAM's terminated with -CF_3 redistribute the energy more slowly along

high-frequency (intra-chain) vibrational modes, resulting in a lower sticking probability.[45] PDMS contains a large number of low-frequency interactions, and so an energy transfer mechanism similar to -CH_3 terminated SAMs may apply. Thus, we conclude that a sticking probability of 30 to 50% is reasonable for a light, inert gas molecule at ambient temperature colliding with a flexible polymer surface. Further study of this type of system, and systems in which there are stronger interactions between the gas and the polymer, would be useful.

The absorption mechanism observed in the MD simulations involves CO_2 interacting with a gap between the polymer chains during a gas-surface collision or while transiently physisorbed, and passing directly into the polymer bulk. The simulations did not show that CO_2 has a strongly preferred adsorption site, i.e. atom type, on the PDMS surface. This is expected for gas-polymer combinations with weak interactions and supports our assumption that every surface atom is an available binding site in the reaction-diffusion simulations. If strong hydrogen bonding were possible, the surface area available for adsorption would be reduced.[46-47] On the other hand, if roughness were significant the surface sites available would be greater than assumed. The MD simulations show that the ratio of the instantaneous surface area to the nominal surface area is 1.1, indicating that the actual, rough, surface area is only 10% greater than the ideally smooth surface assumed in the reaction-diffusion simulations.

C. Simulations of time-dependent permeation

The model framework constructed for phosphorescence quenching (Figure 3) is modified for PDMS permeation by removing the dye quenching kinetics and replacing the glass support with a gas collector volume. A 1 nm thick interfacial region is provided between the polymer and the gas collector, and the desorption steps occur therein; no desorption occurs at the upstream interface in the permeation simulations. The size of the collection compartment is set equal to the experimental collection volume of 41.3 cm^3. The diffusion coefficient of desorbed gases from the interface into the collection chamber is 2.0 m^2/s. The surface site concentration of 1.66 mol/L and the desorption rate constant of 1.4×10^{11} s^{-1} are the same as above. The multi-scale simulation setup is shown in Figure 8. Instrumental characteristics such as volumes and the measured pressure rise in the upstream chamber when gas is initially introduced are included in the model. Because the downstream volume remains at low pressure relative to the surroundings, a small

amount of gas can leak into the collection chamber; this effect is included in the simulations for the sake of completeness. Details on the implementation of this step can be found in the SI Section 9, and relevant values are listed in Table S2.

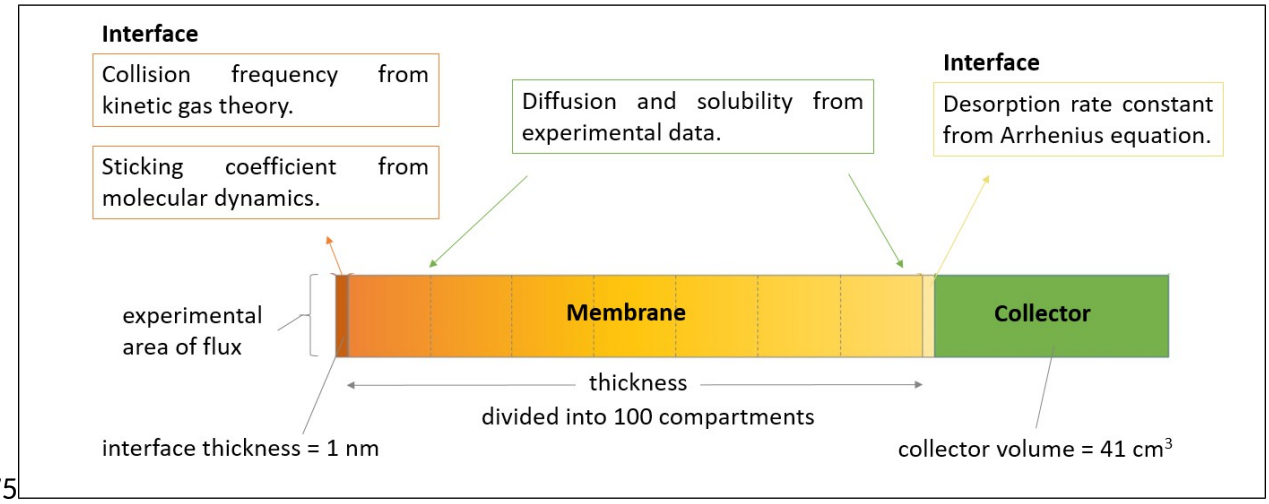

Figure 8. Overview of multi-scale model for a permeation simulation. The membrane is divided into 100 compartments, plus two thin interfacial compartments. An additional compartment collects gas after its permeation. The thickness and area are based on the particular sample being simulated. The surface description is the same as for the dye quenching study, except for the sticking coefficient, which is now known from MD.

The solubility of each gas in PDMS is taken from the literature.[40] The permeability measured under each experimental condition (combination of gas, polymer sample, and upstream pressure) is divided by the literature solubility to calculate the diffusivity. These experimental conditions and the values used in simulation are presented in Table 3. We use the literature value for solubility because solubility varies only over an order of magnitude for a given polymer, whereas the diffusivity within the polymer may vary over six orders of magnitude for different permeants.[48] Only N_2 and CO_2 are presented in the main body, since they represent the lower and upper limits of permeability in PDMS, respectively; similar data for O_2 and CH_4 are available in the SI. The adsorption rate constant is calculated for each p_{up} from Eqn. 2 with $\mu = 0.30$.

Gas	*S* (a)	Sample ID	*l*	*A*	p_{up}	*D*

	mol/(L Pa)		μm	cm^2	kPa	m^2/s
CO_2	5.68×10^{-7}	L4S2	163	0.203	122	2.34×10^{-9}
					206	2.34×10^{-9}
					311	2.39×10^{-9}
N_2	3.96×10^{-8}	L4S2	163	0.203	122	3.27×10^{-9}
					206	3.26×10^{-9}
					416	3.26×10^{-9}
		L5S1	165	0.187	820	2.80×10^{-9}

(a) Reference [40]

Table 3. Input values for multi-scale simulations for comparison to experimental permeation of PDMS.

Experimentally, the upstream permeant gas pressure p_{up} increases over several seconds after opening the gas valve. This rise is captured and used as an input to the simulation rather than assuming an instantaneous pressure step. The beginning of the rise is used as the zero for the simulation time base. The changing internal concentration of the gas in the polymer is set to be proportional to the external pressure, p_{up},

$$[gas_{(p)}] = S\, p_{up} \tag{10}$$

where the proportionality constant, S, is the gas's Henry's law solubility over the pressure range in this study.[40] Figures 9a-c and 10 show the permeation curves from experiment and the corresponding simulations for N_2 and CO_2, respectively, through PDMS for upstream pressures from 122 to 820 kPa. While the experimental standard deviation for samples at higher pressures was not thoroughly investigated, the data are sufficient for comparison to simulation. The figures for N_2 and CO_2 are highlighted here because they represent the extremes in permeability among the gases tested; similar data for O_2 and CH_4 are available in the SI Section 11, Figure S8 and Table S3. The agreement for all times, gas types, and pressures is within experimental error, confirming that the simulation framework and the model represent the full permeation process

over a wide range of conditions, Henry's law solubilities, and permeabilities. More details on implementation of Eq 10 in the model are presented in the SI Section 10, and relevant values are listed in Table S2. The error introduced by ignoring the dynamic solubility increase is illustrated in Figure 9d, in which the results of simulations with instantaneous and dynamic increases in available binding sites are compared. The simulation with a dynamic increase faithfully reproduces the pre-steady-state region of the permeation curve; the simulation with all binding sites instantly available only reproduces the steady-state region of the curve. This dynamic treatment is especially important for the more permeable gases or where the upstream pressure rise takes place over a long time.

The simulations add two new insights to dynamical aspects of the system. First, we find that inclusion of instantaneous increases in the maximum possible concentration of the permeant in the membrane as the permeant pressure increases on the upstream side is required for good agreement between the experimental and calculated pressure rise for all gases studied. This behavior would need to be incorporated in any new theoretical treatment of solution-diffusion in membranes far from steady state. It should be noted that while the computational treatment for single permeants is straightforward, it is likely to be more complex when time-varying mixtures are involved. Second, we find that the bulk PDMS diffusion coefficient is sufficient to describe gas motion at all locations within the polymer. This indicates that tortuosity, polymer chain fluctuations, and other detailed, molecular-level characteristics are well-captured by the Fickian diffusion description, and do not need to be included explicitly.

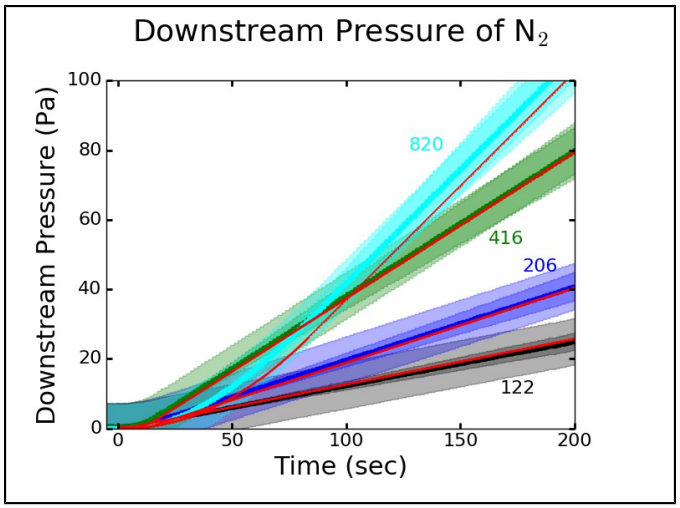

631(a)

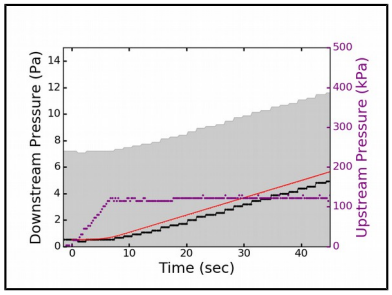

632(b)

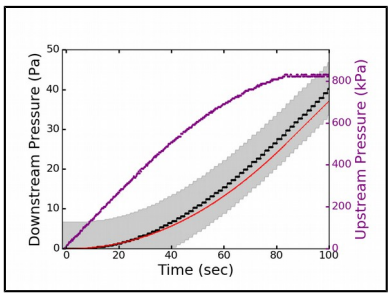

(c)

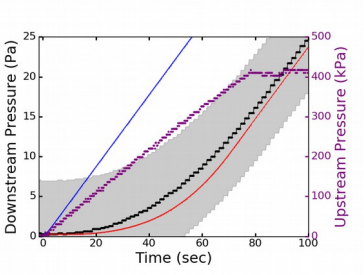

633(d)

634Figure 9. Comparison of simulation and experimental permeation curves for N_2. The simulation
635results are shown in red. (a) Summary plot for all pressures. The shaded regions represent an
636experimental sample-to-sample standard deviation of 10%. Each curve is labeled with the
637upstream pressure in kPa. (b) Pre-steady state detail for p_{up} = 122 kPa (c) Pre-steady state detail
638for p_{up} = 820 kPa. The black curves in (b) and (c) are experimental measurements, and the purple
639curves are the measured upstream pressure rise. The shaded regions represent the accuracy of the
640downstream pressure transducer. The accuracy of the pressure transducer is the main source of
641error at low pressures; at higher pressures, the sample-to-sample variation is the main source of
642error. The lower limit of detection of the downstream pressure detector is 0.1 Pa, resulting in
643steps in the measured downstream pressure. (d) Comparison of simulation with and without a
644dynamic increase in maximum absorbate concentration in the polymer. The experimental data for
645N_2 permeation through sample L5S2 are in black. The upstream pressure rise is in purple. The
646correct simulation, with a dynamic increase in maximum concentration within the polymer, is
647shown in red. The simulation with all internal gas absorption sites available at the start of the
648upstream pressure rise is shown in blue.

(a) 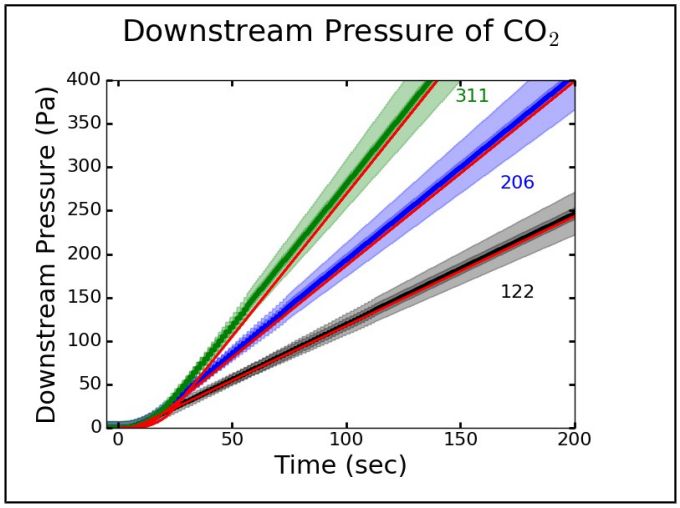

(b) 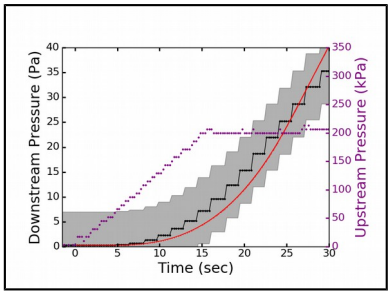

Figure 10. Comparison of simulation and experiment permeation curves for CO_2. The simulation results are shown in red. (a) Summary plot for all pressures. The shaded regions represent an experimental sample-to-sample standard deviation of 10%. Each curve is labeled with the upstream pressure in kPa. (b) Pre-steady state detail for p_{up} = 206 kPa. The black curve is the experimental measurements, and the purple curve is the measured upstream pressure rise. The shaded region represents the accuracy of the downstream pressure transducer. The accuracy of the pressure transducer is the main source of error at low pressures; at higher pressures, the sample-to-sample variation is the main source of error. The lower limit of detection of the downstream pressure detector is 0.1 Pa, resulting in steps in the measured downstream pressure.

VI. Application of the model: predictive simulations for two rubbery membrane separations systems

Two variations of the reaction-diffusion framework developed in this work are used to develop models that account for the entire experimentally observed permeation process, both steady-state and pre-steady-state, for phosphorescence quenching, and gas permeation through a membrane. The models have no adjustable parameters and are physically realistic, and therefore predictive. In this section we take one of the models, gas permeation through PDMS, to examine two other types of systems at an exploratory level: CO_2 separations from air, and solar CO_2 photoelectrochemical reduction. We describe how the system models are set up, then present and discuss the predictions from the simulations.

A. Simulations of CO_2 separation from air

There is currently much interest in use of permeable membranes for CO_2 capture from ambient air[49-50] and we use the PDMS permeation model described above to examine how a membrane with its properties would function. Experimentally, gases have been shown to permeate independently in rubbers.[51-52] Simulation of permeation of a mixture of N_2 and O_2, using the setup shown in Figure 8, agrees with experiment (see SI Sect. 12 and Fig. S9).[52] We apply this model to simulate permeation of mixtures containing several components of dry air: N_2, O_2, Ar, and CO_2. All relevant input values for the simulations are reported in Table S4. In Figure 11a, it is shown that the selectivity for CO_2 in a mixture of gases, all at the same partial pressure, is near to its ideal selectivity (≈10x that of N_2 and ≈5x that of O_2). However, the concentration of CO_2 in air is low, $p(CO_2)$ = 0.041 kPa.[53] If the concentrations of gases are set to their concentrations in air (80 kPa for N_2, 21 kPa for O_2, and 0.95 kPa for Ar),[54] the permeation of CO_2 nearly ceases, due to its extremely low partial pressure, as shown in Figure 11b. The simulations enable a target permeability for CO_2 to be estimated for a membrane that would selectively increase the CO_2 concentration in air. Assuming a CO_2 permeability value 100 times higher than for PDMS, with that for the other gases held constant, enrichment to 24% is predicted. This hypothetical situation is not achievable with a single component polymeric membrane because selectivity and permeability for gases of similar characteristics cannot be tuned independently.[55] To identify useful architectures, the model framework presented here can be extended to evaluate and compare new membrane design concepts prior to experimental study, such as layered and inorganic-organic composites and supported ionic liquids. Information on performance characteristics of these systems under intermittent conditions can be obtained from the simulations.[50]

(a) 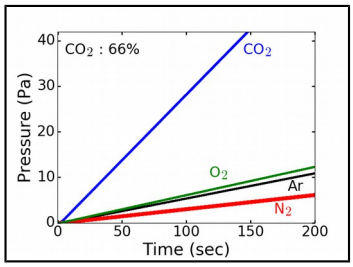

(b) 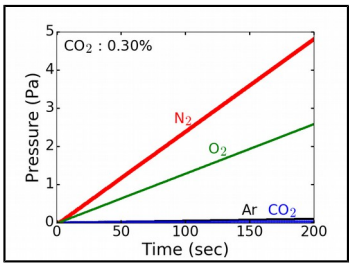

(c) 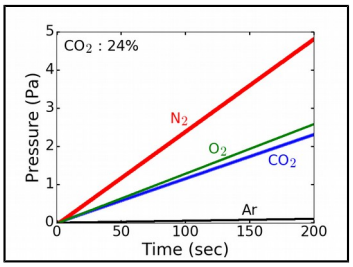

Figure 11. Downstream gas composition for upstream mixtures of O_2, N_2, Ar and CO_2 as a function of time. (a) All four gases present at equal upstream partial pressure, resulting in a downstream mixture highly enriched in CO_2. (b) Upstream gas mixture with the same composition as air permeating PDMS; minimal CO_2 permeation is observed due to its low upstream concentration. (c) Upstream gas mixture with the same composition as air permeating a hypothetical polymer with CO_2 permeability 100 times greater than PDMS, resulting in the downstream gas mixture containing 24% CO_2.

B. Simulations of solar CO_2 reduction product crossover between electrode chambers during a diurnal cycle

Solar fuels generators[56] utilize membranes to separate the cathode and anode regions, and enable ion transfer between catholyte and anolyte during operation. For an example of the device architecture, see Reference [57]. Reduced products are formed on the cathode side, and oxygen is formed on the anode side. The basic architecture of the commercial membranes used for solar hydrogen generators is a phase-separated polyelectrolyte with glassy regions that are impermeable to H_2 and O_2, typically dissolved in electrolyte or present as gas bubbles, and hydrated channels with good ionic conductivity.[58-59] A recent modeling study has shown that the H_2 and O_2 product crossover-blocking property of a membrane for a photoelectrochemical hydrogen generation system is crucial for efficient operation, and can be achieved by reducing conductivity since the crossover path is typically through the hydrated ionic conduction channels.[60]

Solar photoelectrochemical devices that convert CO_2 into reduced hydrocarbon and oxygenate products present a much more complicated situation. They usually generate mixtures on the cathode side, where each product may influence the others' transport processes through the membrane, and O_2 on the anode side, which can diffuse in the opposing direction. In a solar CO_2 reduction device (illustrated in Figure 12a), the rate of product formation and the chemical composition of the products are voltage-dependent. The cell voltage is determined by the amount of sunlight incident on the light absorber in the device, varying with time of day, season, and weather.[61] It cannot be assumed that steady-state membrane operation is ever achieved; however multiphysics models generally do so because of the lack of information about their non-steady-state transport.[62] The glassy matrix blocks significant permeant crossover, but exposure of glassy polymers to CO_2 can cause them to plasticize, resulting in development of a rubbery character over time with increased permeability, and product crossover between the electrodes' chambers.[55, 60] This will potentially reduce efficiency and selectivity of these systems. Modeling

studies examining optimum membrane characteristics for CO_2 reduction systems have not been reported to our knowledge.

The model developed in the present work for PDMS permeated by CH_4, a prototypical CO_2 reduction product, allows aspects of varying production rate and cross-over to be examined. Assumption of PDMS-like properties is a worst-case scenario, representing a membrane that has been extensively plasticized in use. The primary modification of the kinetic processes in the model is to change the simulated system from a gas-membrane system to an aqueous electrolyte-membrane system. Under such conditions, the interfacial interactions change, but transport within the membrane is unaltered if swelling and water uptake are negligible. The simulation setup for this case is shown in Figure 12b. The surface adsorption rate constant k_{ads} (see Reaction I) is calculated from the Smoluchowski equation for diffusion-controlled reactions, rather than as a scattering process as in the gas-polymer case. Using the diffusion coefficient of methane in water of 2.35×10^{-9} m^2/s (at 308 K)[63] and an interaction distance of 4 Å, which is twice the van der Waals radius, k_{ads} is equal to 7×10^9 M^{-1} s^{-1}. The diffusion coefficient of CH_4 molecules between electrolyte and interface compartments is set to 1 m^2/s to represent a rapidly stirred electrolyte. It is assumed that once the permeant has traversed the membrane, it does not back-diffuse. It also assumed that the catholyte is well mixed but not recirculated, allowing products to accumulate.

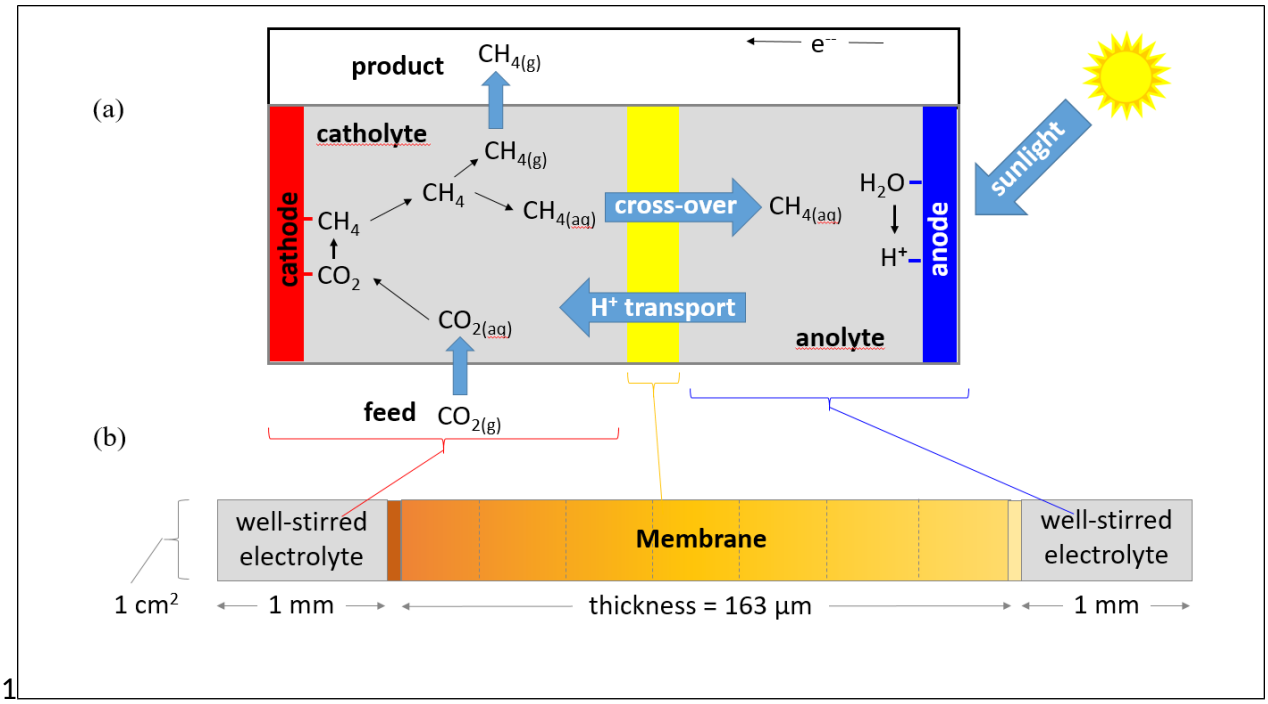

Figure 12. Overview of a solar fuels device and its multi-scale model. (a) An example of a solar fuels device with a face-to-face architecture, in which the cathode, anode, and membrane all have the same area, and the membrane is separated from the catalyst layers by aqueous electrolyte. The reduction of CO_2 to CH_4 is shown, including electron transport, proton transport, carbon dioxide transport, carbon dioxide reduction reaction, and methane desorption, along with the possibilities for CH_4 to become hydrated and cross over the membrane or to enter gas phase and be collected in the product stream. Protons for the reduction reaction are generated at the anode via a water-splitting reaction. Details of the proton transport depend upon the pH, the buffer system, and the membrane type, and are omitted here. (b) In the multi-scale model, the catalysts are combined with their electrolyte regions to form a single well-stirred electrolyte compartment. The catholyte compartment contains a simplified version of all the chemistry occurring at the cathode surface, representing all the reactive steps and the desorption step by a single step for methane production. No chemistry occurs in the simulated anode region, which serves simply as a collection compartment for CH_4 in this work. The geometry is that of a typical solar fuels device prototype with 1 cm^2 cross-sectional area and 1 mm thick electrolyte compartments. The interfacial regions between electrolyte and membrane are 1 nm thick.

If only CH_4 is produced at a typical current density for a solar photoelectrochemical device of 0.010 A/cm^2, a production rate of 13×10^{-9} mol/(cm^2 s) is expected assuming the catalyst area is equal to the geometric area of the cathode.[64] For the combined cathode-catholyte region used in the simulations, the CH_4 production rate per area converts to a volumetric production rate of χ_{prod} = 1.30×10^{-4} mol/(L s). Because photocurrent scales with time of day, the rate of CH_4 production would be at its maximum only when insolation is at its maximum.[61] For simplicity, this diurnal

variation is described as a simple triangle wave lasting a total of 8 hours, shown in Figure 13a. An extended period of darkness follows during which no additional CH_4 is produced but that which remains dissolved in the electrolyte can permeate the membrane. The CH_4 production reaction step is implemented as a pseudo-0th order reaction

$$\xrightarrow{k} cathode + CH_4 \quad (cathode) \tag{VII}$$

where $k'_{prod} = r_{sun} \times \chi_{prod}$, and r_{sun} is the ratio of current sunlight level to the maximum amount of sunlight. This representation is used because it allows a correct generation rate without specifying detailed surface kinetics. Once formed, methane may dissolve up to its solubility limit in water of 0.001 M (for 308 K),[65] represented as an aqueous solution site, "aq-site,"

$$CH_4 + aq\text{-}site \xrightarrow{k_{hyd}} CH_{4(aq)} \tag{VIII}$$

or bubble out of solution as a gas

$$CH_4 \xrightarrow{k_{bub}} CH_{4(g)} \tag{IX}$$

where the zeroth order rate constants (now equal to the rates) for hydration, $k_{hyd} = 10^{50}$ mol/(L s), and bubbling out, $k_{bub} = 10^{25}$ mol/(L s), are arbitrarily high to represent nearly instantaneous processes. The larger rate constant for hydration ensures that the methane molecules remain in water if an aqueous site is available; if no site is available, the methane molecule will bubble out of solution instead. It is assumed that the electrolyte is rapidly stirred such that boundary layer and mass transport limitations are negligible.

The transport properties of CH_4 in PDMS and two hypothetical polymers (Hyp1 and Hyp2) are listed in Table 4. Both hypothetical polymers have a permeability three orders of magnitude lower than PDMS. For Hyp1, all reduction in permeability comes from a reduction in the diffusivity; for Hyp2, all reduction in permeability comes from a reduction in the solubility. As a point of reference, the values of *D* and *S* for Hyp1 are similar to those for polystyrene.[66]

Polymer	*S*	*D*	P_m
	(mol/L)/(mol/L) (a)	m^2/s	m^2/s
PDMS (b)	0.467	2.20×10^{-9}	1.03×10^{-9}
Hyp1	0.467	2.20×10^{-12}	1.03×10^{-12}

Hyp2	4.67×10^{-4}	2.20×10^{-9}	1.03×10^{-12}

(a) The units for solubility are mol/L inside of the polymer per mol/L in the external electrolyte.

(b) Reference [40]

Table 4. Properties of the membranes used in the diurnal cycle simulations.

(a)

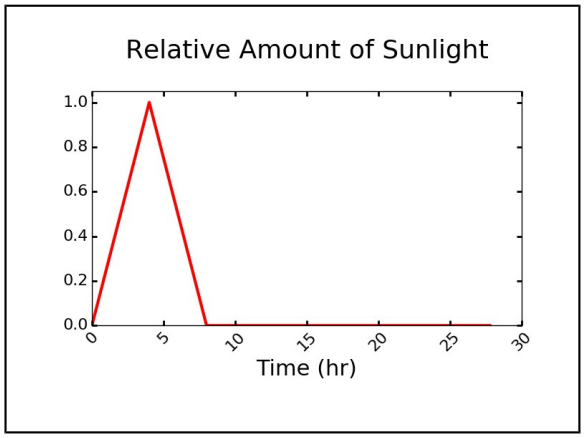

(b)

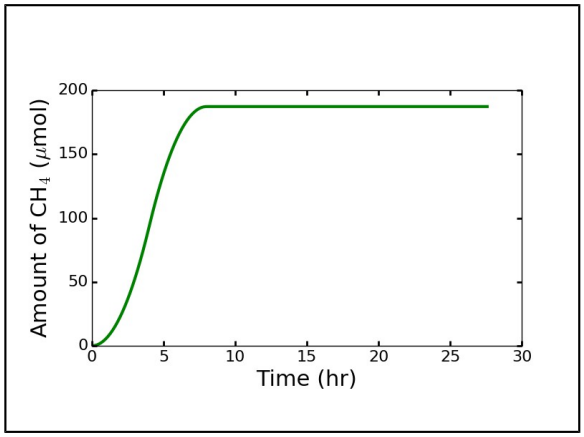

Figure 13. The production of CH_4. (a) The normalized level of sunlight, which is a multiplier for the rate constant for CH_4 production. (b) The total amount of CH_4 produced from Reaction VII, including both those that will become gaseous and those that will become hydrated.

The amount of CH_4 produced from Reaction VII over time is shown in Figure 13b and is the same for all three simulations. The rate of CH_4 production increases over the first four hours, reaches its maximum at the peak of available sunlight, then declines over the next four hours, resulting in a total production of 1.87×10^{-4} moles of CH_4. Because the solubility limit for gases

in water is low, a constant aqueous concentration of CH_4 is rapidly established, as shown for PDMS, Hyp1, and Hyp2 in Figure 14a, 14d, and 14g, respectively. Additional CH_4 produced bubbles out as a gaseous product, as shown for PDMS, Hyp1, and Hyp2 in Figure 14b, 14e, and 14h, respectively. For a theoretical, completely blocking membrane, the maximum aqueous concentration is reached in 7.8 minutes. Hyp1 and Hyp2 come close to this, with aqueous phase saturation occurring within 10 minutes, at which time, sunlight is less than 10% of its maximum level. The concentration profiles of CH_4 within all three membranes are available in the SI Section 13, Figure S10. The concentration profile of CH_4 within the hypothetical membranes also reaches steady state within 10 minutes. In PDMS, these processes take 20 minutes. The delay in reaching steady state, compared to the hypothetical membranes, is due to the high permeability of PDMS. As CH_4 is entering the aqueous phase near the cathode, it is also being removed by transport across the membrane, thus delaying the build-up to its maximum concentration. However, this build-up is only a small fraction of the device's operating time.

Once CH_4 production ceases, it takes only about 1 minute for the remaining CH_4 to traverse the PDMS membrane into the anode chamber. This means that for a very permeable membrane, any CH_4 present in the aqueous phase will cross over the membrane. In contrast, the depletion of CH_4 from the catholyte and emptying of the remaining CH_4 within the membrane is estimated to take over 40 hours for the less permeable membranes. In this case, the enhanced blocking capabilities of these membranes are due not only to lower steady-state permeability but also retention of product within the membrane during dark hours, as can be seen in the concentration profiles in the SI Section 13, Figure S10. The membrane is a key contributor to the ability to recover products from solar fuels devices. The maximum possible amount of product that can be recovered is equal to the total amount of gas produced, shown for PDMS, Hyp1, and Hyp2 in Figure 14b, 14e, and 14h, respectively. Conversely, the total amount of methane cross-over for PDMS, Hyp1, and Hyp2 are shown in Figure 14c, 14f, and 14i, respectively. For PDMS, ≈10% of CH_4 crosses the membrane. Because CH_4 is highly permeable in PDMS, 25% represents an approximate upper bound on gaseous product loss, though products with higher solubility in water may experience even greater losses. By reducing the permeability by three orders of magnitude, recovery can be increased to 99.96%. It does not matter whether this decrease in permeability results from changes in diffusivity or solubility. Even with low permeability, however, it is unlikely that product cross-over can be prevented completely.

This is an interesting situation because the solar-fuels device is operating under continually changing conditions, so the rate of methane production is changing continually as well. However, the aqueous concentration of methane is constant over most of the operating time, and the membrane is essentially experiencing steady-state conditions with respect to this permeant during daylight hours. Using a more realistic insolation profile or including the fluctuations in sunlight that are present under real-world operating conditions will have little effect on the operation of the membrane, at least for the conditions studied herein. Fluctuations in sunlight levels may play a greater role in other types of systems, for example, when the production rate is lower, the aqueous solubility is higher, or the permeability is higher.

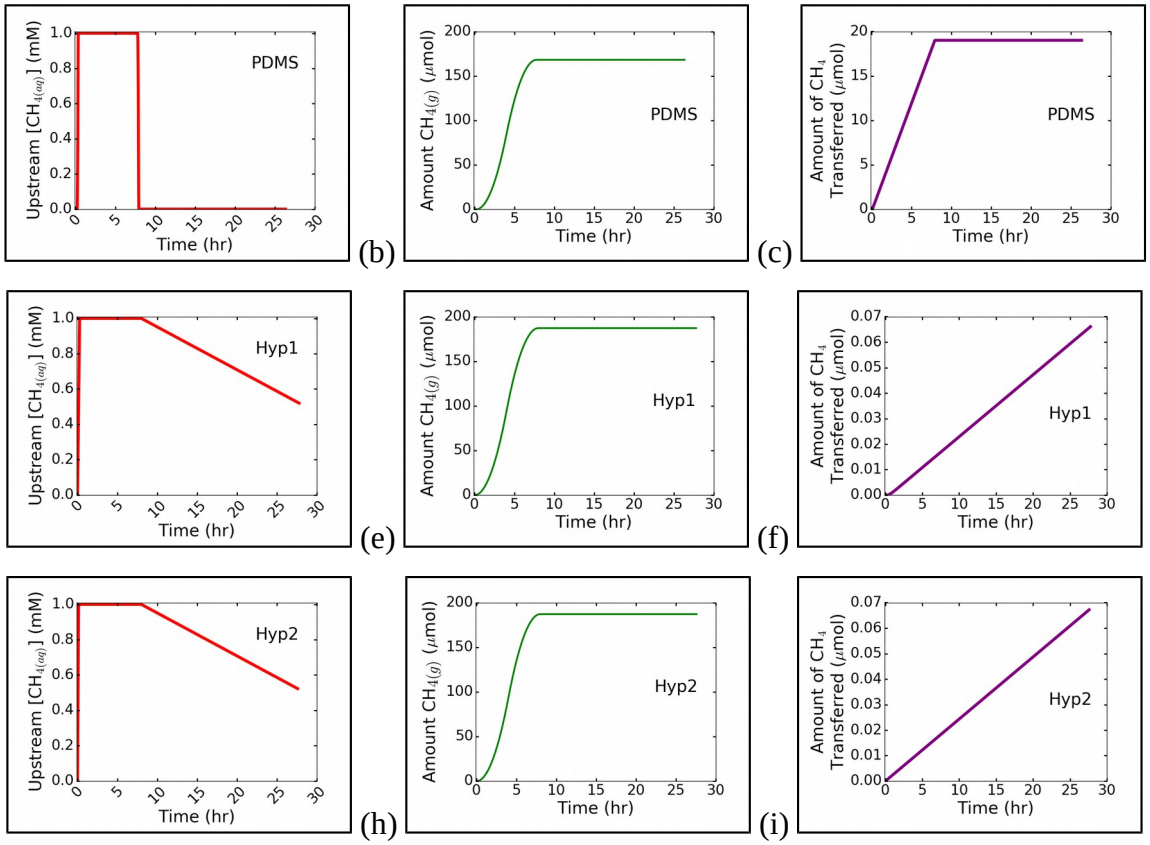

Figure 14. Results of membrane crossover simulations during diurnal photoelectrochemical CH_4 production. (a) – (c) PDMS, (d) – (f) Hyp1, (g) – (i) Hyp2. (a), (d), (g) Upstream concentration of dissolved CH_4 in the cathode chamber stays at the aqueous solubility limit during insolation. The remaining CH_4 is rapidly depleted by crossing the PDMS membrane but is slowly depleted for the two hypothetical membranes due to their low permeability. (b), (e), (h) Amount of CH_4 that enters the gas phase and can be collected as a product. (c), (f), (i) Amount of CH_4 that

crosses over the membrane and so is not collected as product. The results for the two hypothetical membranes are nearly identical due to their identical permeabilities.

VII. Summary and conclusions

In this work we describe a multiscale modeling study of permeation of rubbery polymer membranes by simple inert solutes, with the goal of developing a full description of steady-state and non-steady-state processes. We have chosen to focus on these systems as a simplest case since the polymer transport properties, solubility and diffusivity, are expected to be constant over time. We have confirmed that the permeation process is insensitive to permeant adsorption and absorption kinetics in these systems, consistent with the assumption made in the solution-diffusion model for membrane permeation. Two quantitatively validated models, built on a common reaction-diffusion framework, are reported: quenching of PtOEP phosphorescent dye in C4PTP, an oxygen sensor system, and permeation of O_2, N_2, CH_4 and CO_2 through a PDMS separator. The predictive framework is extended to simulate two additional hypothetical systems, separation of CO_2 from air using a PDMS-like membrane, and crossover of the CO_2 reduction product, CH_4, in a solar-fuels system whose membrane separator is rubbery or glassy, but inert to the permeant.

Because the goal is the development of a quantitatively predictive model with no adjustable parameters, the model construction process is dependent on time-dependent permeation data as well as experimental and theoretical information on specific materials properties and processes. Such data are not commonly available in the literature so experimental and MD computational studies have been performed and are reported in this paper. The results show that a simple reaction-diffusion framework simulated using stochastic methods is adequate to capture the details of interfacial processes as well as bulk processes, covering a broad range of length- and timescales. Measured quantities such as solubilities and diffusion coefficients contain enough information about solute-polymer interactions to predict experimental observables such as pressure increases and phosphorescence quenching as investigated here without explicit inclusion of free volume dynamics and tortuosity, although these elements can be built into the model with straightforward modifications.

Several new insights to polymer-permeant systems have been obtained through the simulations.

(i) Time-dependent phosphorescence quenching is related in a complicated way to the amount of O_2 sorbed into a polymer due to the rate mismatch between dye-O_2 interactions and O_2 transport. This suggests that such sensors are best used in conjunction with models such as that presented here to ensure complete data interpretation.

(ii) The pre-steady state portion of a gas permeation curve contains a great deal of information about the nature of the gas-polymer interaction. In particular, we find it necessary to include a dynamically increasing maximum concentration within the polymer as the upstream permeant pressure increases, in accordance with Henry's law solubility, to reproduce the experimental data successfully. This raises interesting questions about what is occurring inside the polymer during a pressure rise, especially how interfacial processes affect the polymer bulk, and how fast this response is.

(iii) During intermittent operation such as a diurnal cycle, low-permeability membranes can continue to permit crossover long after product formation has ceased due to slow permeation of residual products in the electrolyte. This effect needs to be taken into account for successful membrane and separation systems design for complex situations such as solar fuels generators and CO_2 capture.

Declaration of interest

Conflicts of interest: none

Supplementary Information

Supplementary data related to this article can be found at http:// *link*

Data tables for all figures and additional experimental data can be found in the spreadsheets at *https://doi.org/10.5072/FK2Z31W208*

Acknowledgements

This material is based upon work performed by the Joint Center for Artificial Photosynthesis, a DOE Energy Innovation Hub, as follows: The reaction-diffusion simulations were performed by M. S. and F. H., and experimental measurements were performed by M. T. and A. W., supported through the Office of Science of the U.S. Department of Energy under Award Number DE-SC0004993. M. T. thanks the National Science Foundation Graduate Research Fellowship under Grant No. DGE 1106400. D. B., B. M. and W. A. G. acknowledge funding from Borsch Energy Research for the MD simulation work. Borsch Energy Research had no involvement in decisions concerning data collection, data processing, writing, or article submission. The authors are grateful to Dr. Daniel J. Miller (JCAP, LBNL) for many helpful discussions on membrane polymer science, to Mr. Ezra L. Clark (JCAP, LBNL) for data on photoelectrochemical production of methane, and to Dr. William D. Hinsberg (Columbia Hill Technical Consulting) for discussions on the use of Kinetiscope in this work.

References

1. Mulder, M., *Basic Principles of Membrane Technology*. Kluwer Academic Publishers: Dordrecht, The Netherlands, 1996.
2. Wijmans, J. G.; Baker, R. W., The Solution-Diffusion Model - a Review. *J Membrane Sci* **1995,** *107* (1-2), 1-21.
3. Crank, J.; Park, G. S., *Diffusion in Polymers*. Academic Press Inc., Ltd.: London and New York, 1968.
4. Shin, D. W.; Guiver, M. D.; Lee, Y. M., Hydrocarbon-Based Polymer Electrolyte Membranes: Importance of Morphology on Ion Transport and Membrane Stability. *Chem Rev* **2017,** *117* (6), 4759-4805.
5. Kusoglu, A.; Weber, A. Z., Study of PFSA ionomers using X-ray scattering techniques. *Abstr Pap Am Chem S* **2014,** *248*.
6. Jayarajah, C. N. Luminescence Quenching Studies of Oxygen Dinusion in Highly Permeable Media. University of Toronto, 1998.
7. Jayarajah, C. N.; Yekta, A.; Manners, I.; Winnik, M. A., Oxygen diffusion and permeability in alkylaminothionylphosphazene films intended for phosphorescence barometry applications. *Macromolecules* **2000,** *33* (15), 5693-5701.
8. Wang, X.-d.; Wolfbeis, O. S., Optical methods for sensing and imaging oxygen: materials, spectroscopies and applications. *Chemical Society Reviews* **2014,** *43*, 3666-761.
9. Bunker, D.; Garrett, B.; Kleindienst, T.; III, G. L., Discrete simulation methods in combustion kinetics. *Combustion and Flame* **1974,** *23*, 373-379.
10. Gillespie, D. T., General Method for Numerically Simulating Stochastic Time Evolution of Coupled Chemical-Reactions. *J Comput Phys* **1976,** *22* (4), 403-434.
11. Hinsberg, W. D.; Houle, F. A., *Kinetiscope*. www.hinsberg.net/kinetiscope. , 2015.
12. Houle, F. A.; Hinsberg, W. D.; Morrison, M.; Sanchez, M. I.; Wallraff, G.; Larson, C.; Hoffnagle, J., Determination of coupled acid catalysis-diffusion processes in a positive-tone chemically amplified photoresist. *Journal of Vacuum Science & Technology B: Microelectronics and Nanometer Structures* **2000,** *18*, 1874.
13. Houle, F. A.; Hinsberg, W. D.; Sanchez, M. I., Kinetic Model for Positive Tone Resist Dissolution and Roughening. *Macromolecules* **2002,** *35*, 8591-8600.
14. Wiegel, A. A.; Wilson, K. R.; Hinsberg, W. D.; Houle, F. A., Stochastic methods for aerosol chemistry: a compact molecular description of functionalization and fragmentation in the heterogeneous oxidation of squalane aerosol by OH radicals. *Phys. Chem. Chem. Phys.* **2015,** *17*, 4398-4411.
15. Wiegel, A. A.; Liu, M.; Hinsberg, W. D.; Wilson, K. R.; Houle, F. A., Diffusive Confinement of Free Radical Intermediates in the OH Radical Oxidation of Semisolid Aerosol. *Physical Chemistry Chemical Physics* **2017,** *19*, 6814-6830.
16. Wallraff, G.; Hutchinson, J.; Hinsberg, W.; Houle, F.; Seidel, P.; Johnson, R.; Oldham, W., Thermal and acid-catalyzed deprotection kinetics in candidate deep ultraviolet resist materials. *Journal of Vacuum Science & Technology B: Microelectronics and Nanometer Structures* **1994,** *12* (6), 3857-3857.
17. Houle, F. A.; Hinsberg, W. D.; Sanchez, M. I.; Hoffnagle, J. A., Influence of resist components on image blur in a patterned positive-tone chemically amplified photoresist. *Journal*

of Vacuum Science & Technology B: Microelectronics and Nanometer Structures **2002,** *20* (3), 924-924.
18. Bowers, K.; Chow, E.; Xu, H.; Dror, R.; Eastwood, M.; Gregersen, B.; Klepeis, J.; Kolossvary, I.; Moraes, M.; Sacerdoti, F.; Salmon, J.; Shan, Y.; Shaw, D., Scalable Algorithms for Molecular Dynamics Simulations on Commodity Clusters. *ACM/IEEE SC 2006 Conference (SC'06)* **2006,** (November), 43-43.
19. Shivakumar, D.; Williams, J.; Wu, Y.; Damm, W.; Shelley, J.; Sherman, W., Prediction of Absolute Solvation Free Energies using Molecular Dynamics Free Energy Perturbation and the OPLS Force Field. *Journal of Chemical Theory and Computation* **2010,** *6*, 1509-1519.
20. Guo, Z.; Mohanty, U.; Noehre, J.; Sawyer, T. K.; Sherman, W.; Krilov, G., Probing the α-Helical Structural Stability of Stapled p53 Peptides: Molecular Dynamics Simulations and Analysis. *Chem. Biol. Drug Des.* **2010,** *75*, 348-359.
21. Banks, J. L.; Beard, H. S.; Cao, Y.; Cho, A. E.; Damm, W.; Farid, R.; Felts, A. K.; Halgren, T. A.; Mainz, D. T.; Maple, J. R.; Murphy, R.; Philipp, D. M.; Repasky, M. P.; Zhang, L. Y.; Berne, B. J.; Friesner, R. A.; Gallicchio, E.; Levy, R. M., Integrated Modeling Program, Applied Chemical Theory (IMPACT). *Journal of Computational Chemistry* **2005,** *26* (16), 1752-1780.
22. McQuarrie, D. A., *Statistical Mechanics*. University Science Books: Mill Valley, CA, 2000; p 641.
23. Martyna, G. J.; Tobias, D. J.; Klein, M. L., Constant pressure molecular dynamics algorithms. *Journal of Chemical Physics* **1994,** *101* (5), 4177-4177.
24. Shin, H.; Pascal, T. A.; Goddard, W. A.; Kim, H., Scaled effective solvent method for predicting the equilibrium ensemble of structures with analysis of thermodynamic properties of amorphous polyethylene glycol-water mixtures. *Journal of Physical Chemistry B* **2013,** *117* (3), 916-927.
25. *Polymer Data Handbook*. Oxford University Press: 1999; p 1012.
26. Willard, A. P.; Chandler, D., Instantaneous liquid interfaces. *Journal of Physical Chemistry B* **2010,** *114* (5), 1954-1958.
27. Julin, J.; Shiraiwa, M.; Miles, R. E. H.; Reid, J. P.; Pöschl, U.; Riipinen, I., Mass accommodation of water: Bridging the gap between molecular dynamics simulations and kinetic condensation models. *Journal of Physical Chemistry A* **2013,** *117* (2), 410-420.
28. Julin, J.; Winkler, P. M.; Donahue, N. M.; Wagner, P. E.; Riipinen, I., Near-Unity Mass Accommodation Coefficient of Organic Molecules of Varying Structure. *Environmental Science & Technology* **2014,** *48*, 12083-12089.
29. *Springer Handbook of Materials Measurement Methods*. Springer: Berlin, 2006; p 1207.
30. "Model Super TJE: Ultra Precision Pressure Transducer." HoneyWell. https://measurementsensors.honeywell.com/Pages/Product.aspx?category=&cat=Honeywell&pid=stje (accessed March 24, 2017).
31. "Baratron General Purpose Capacitance Manometers: 750C11T." MKS Instruments. https://www.mksinst.com/product/product.aspx?ProductID=126 (accessed March 24, 2017).
32. Hodge, K.; Prodpran, T.; Shenogina, N. B.; Nazarenko, S., Diffusion of oxygen and carbon dioxide in thermally crystallized syndiotactic polystyrene. *Journal of Polymer Science Part B: Polymer Physics* **2001,** *39*, 2519-2538.
33. Bansal, A. K.; Holzer, W.; Penzkofer, A.; Tsuboi, T., Absorption and emission spectroscopic characterization of platinum-octaethyl-porphyrin (PtOEP). *Chemical Physics* **2006,** *330* (1-2), 118-129.

34. Engel, T.; Reid, P., *Thermodynamics, Statistical Thermodynamics, & Kinetics*. 2nd ed.; Prentice Hall: 2010; p 602.
35. Somorjai, G. A.; Li, Y., *Introduction to Surface Chemistry and Catalysis*. Wiley: 2010; p 800.
36. Atkins, P.; de Paula, J., *Physical Chemistry*. 8th ed.; W. H. Freeman and Co.: New York, USA, 2006; p 1053.
37. Houston, P., *Chemical kinetics and reaction dynamics*. Dover Publications, Inc.: Mineola, New York, 2001; p 518.
38. Dienel, T.; Proehl, H.; Fritz, T.; Leo, K., Novel near-infrared photoluminescence from platinum(II)-porphyrin (PtOEP) aggregates. *Journal of Luminescence* **2004,** *110*, 253-257.
39. Yekta, A.; Masoumi, Z.; Winnik, M. A., Luminescence measurements of oxygen permeation and oxygen diffusion in thin polymer films. *Canadian Journal of Chemistry* **1995,** *73* (11), 2021-2029.
40. Merkel, T. C.; Bondar, V. I.; Nagai, K.; Freeman, B. D.; Pinnau, I., Gas sorption, diffusion, and permeation in poly(dimethylsiloxane). *Journal of Polymer Science, Part B: Polymer Physics* **2000,** *38* (3), 415-434.
41. Brandão, L.; Madeira, L. M.; Mendes, A. M., Mass transport on composite dense PDMS membranes with palladium nanoclusters. *Journal of Membrane Science* **2007,** *288* (1-2), 112-122.
42. Berean, K.; Ou, J. Z.; Nour, M.; Latham, K.; McSweeney, C.; Paull, D.; Halim, A.; Kentish, S.; Doherty, C. M.; Hill, A. J.; Kalantar-zadeh, K., The effect of crosslinking temperature on the permeability of PDMS membranes: Evidence of extraordinary CO2 and CH4 gas permeation. *Separation and Purification Technology* **2014,** *122*, 96-104.
43. Lancaster, D. K.; Johnson, A. M.; Burden, D. K.; Wiens, J. P.; Nathanson, G. M., Inert gas scattering from liquid hydrocarbon microjets. *Journal of Physical Chemistry Letters* **2013,** *4* (18), 3045-3049.
44. Lu, J. W.; Morris, J. R., Gas-Surface scattering dynamics of CO2, NO2, and O3 in collisions with model organic surfaces. *Journal of Physical Chemistry A* **2011,** *115*, 6194-6201.
45. Alexander, W. a.; Zhang, J.; Murray, V. J.; Nathanson, G. M.; Minton, T. K., Kinematics and dynamics of atomic-beam scattering on liquid and self-assembled monolayer surfaces. *Faraday Discussions* **2012,** *157*, 355-374.
46. Donaldson, D. J., Adsorption of Atmospheric Gases at the Air−Water Interface. I. NH 3. *Journal of Physical Chemistry A* **1999,** *103* (1), 62-70.
47. Ogasawara, H.; Horimoto, N.; Kawai, M., Ammonia adsorption by hydrogen bond on ice and its solvation. *Journal of Chemical Physics* **2000,** *112* (19), 8229-8232.
48. Yampolskii, Y. P.; Pinnau, I.; Freeman, B. D., *Materials Science of Membranes for Gas and Vapor Separation*. John Wiley & Sons Ltd: West Sussex, England, 2006; p 445-445.
49. House, K. Z.; Baclig, A. C.; Ranjan, M.; van Nierop, E. A.; Wilcox, J.; Herzog, H. J., Economic and energetic analysis of capturing CO2 from ambient air. *Proceedings of the National Academy of Sciences* **2011,** *108* (51), 20428-20433.
50. Jones, C. W., CO(2) capture from dilute gases as a component of modern global carbon management. *Annual review of chemical and biomolecular engineering* **2011,** *2*, 31-52.
51. Dhingra, S. S.; Marand, E., Mixed gas transport study through polymeric membranes. *Journal of Membrane Science* **1998,** *141*, 45-63.
52. Wu, F.; Li, L.; Xu, Z.; Tan, S.; Zhang, Z., Transport study of pure and mixed gases through PDMS membrane. *Chemical Engineering Journal* **2006,** *117*, 51-59.

53. "Recent Global CO2." Earth System Research Laboratory Global Monitoring Division. https://www.esrl.noaa.gov/gmd/ccgg/trends/global.html (accessed June 16, 2017).
54. IUPAC, *Compendium of Chemical Terminology, 2nd ed*. Blackwell Scientific Publications: Oxford, 1997; Vol. 2017.
55. Sanders, D. F.; Smith, Z. P.; Guo, R.; Robeson, L. M.; McGrath, J. E.; Paul, D. R.; Freeman, B. D., Energy-efficient polymeric gas separation membranes for a sustainable future: A review. *Polymer* **2013,** *54* (18), 4729-4761.
56. Xiang, C.; Weber, A. Z.; Ardo, S.; Berger, A.; Chen, Y. K.; Coridan, R.; Fountaine, K. T.; Haussener, S.; Hu, S.; Liu, R.; Lewis, N. S.; Modestino, M. A.; Shaner, M. M.; Singh, M. R.; Stevens, J. C.; Sun, K.; Walczak, K., Modeling, Simulation, and Implementation of Solar-Driven Water-Splitting Devices. *Angewandte Chemie - International Edition* **2016,** *55* (42), 12974-12988.
57. Singh, M. R.; Clark, E. L.; Bell, A. T., Effects of electrolyte, catalyst, and membrane composition and operating conditions on the performance of solar-driven electrochemical reduction of carbon dioxide. *Physical Chemistry Chemical Physics* **2015,** *17* (29), 18924-18936.
58. Allen, F. I.; Comolli, L. R.; Kusoglu, A.; Modestino, M. A.; Minor, A. M.; Weber, A. Z., Morphology of hydrated as-cast Nafion revealed through cryo electron tomography. *ACS Macro Letters* **2015,** *4* (1), 1-5.
59. Kusoglu, A.; Weber, A. Z., New Insights into Perfluorinated Sulfonic-Acid Ionomers. *Chemical Reviews* **2016,** *117*, 987-1104.
60. Berger, A.; Segalman, R. A.; Newman, J., Material requirements for membrane separators in a water-splitting photoelectrochemical cell. *Energy & Environmental Science* **2014,** *7* (4), 1468-1476.
61. Chen, Y.; Lewis, N. S.; Xiang, C., Modeling and Simulation of the Spatial and Light-Intensity Dependence of Product Distributions in an Integrated Photoelectrochemical CO 2 Reduction System. *ACS Energy Letters* **2016,** *1* (1), 273-280.
62. Stevens, J. C.; Weber, A. Z., A Computational Study of Optically Concentrating, Solar-Fuels Generators from Annual Thermaland Fuel-Production Efficiency Perspectives. *Journal of The Electrochemical Society* **2016,** *163* (7), H475-H484.
63. Jähne, B.; Heinz, G.; Dietrich, W., Measurement of the diffusion coefficients of sparingly soluble gases in water. *Journal of Geophysical Research: Oceans* **1987,** *92* (C10), 10767-10776.
64. Clark, E. L., personal communication. 2016.
65. Clever, H. L.; Young, C. L., *"Methane." IUPAC Solubility Data Series*. Pergamon Press: Oxford, England, 1987; Vol. 27/28.
66. Rein, D. H.; Baddour, R. F.; Cohen, R. E., Gas solubility and diffusion in a polystyrene-polybutadiene block copolymer. *Journal of Applied Polymer Science* **1992,** *45* (7), 1223-1227.